JOURNAL OF GEOPHYSICAL RESEARCH, VOL. 99, NO. A5, PAGES 8705–8730, MAY 1, 1994

Magnetotail views at $33R_E$: IMP 8 magnetometer observations

Zerefsan Kaymaz[1] and George L. Siscoe[1]
Department of Atmospheric Sciences, University of California, Los Angeles

Nikolai A. Tsyganenko and Ronald P. Lepping
NASA Goddard Space Flight Center, Greenbelt, Maryland

Abstract. This paper presents magnetic field vector (**B**) maps, electric current vector (curl **B**) maps, magnetic force (**JxB**) contour maps, and total field contour maps covering the full tail cross section in the *yz* plane. The maps are based on 16 years of 5-min averages of IMP 8 magnetic field data. During this time, IMP 8 traversed the tail between -25R_E and -40R_E in the *x* direction. Its average *x* distance was -33R_E. For this average distance we show separate maps for low and high dipole tilts, corresponding to equinox and northern hemisphere summer seasons. The low-tilt (equinox) maps show symmetrical field and current patterns; the high-tilt (solstice) maps show the cross-tail current sheet arcing above the equatorial diagonal in the center and dipping below it on the flanks. The shape of warped current sheet fits Fairfield's (1980) displaced ellipse model fairly well. The distance at which the current sheet is hinged to the magnetic equator is found to be 9.88R_E and is independent of *Kp*. The *z* profile of current density shows a central peak, 3R_E full width at half maximum, and smaller, flanking shoulders. A Harris sheet profile with a 7R_E thickness fits the B_x profile. Though these are magnetic field data, the **JxB** maps clearly outline the plasma sheet. This approach also gives a 7R_E thickness. Many of the average field and current features inferred and demonstrated in earlier studies are confirmed here; some of them are seen for the first time in full cross-section view. Among new features revealed are a large current vortex in the winter hemisphere lobe, a dawn-dusk asymmetry in the **JxB** force in the plasma sheet (it is stronger on the duskside), and a separation of the cross-tail current sheet into core and wing parts.

1. Introduction

In the quarter century since *Ness* [1965] published the first exploratory map of the geotail, more than a dozen tail-probing satellites (the Explorers, the Velas, the IMPs, the ISEEs, and others, most recently, Geotail) have surveyed its depth, length, and breadth. Deep space probes (the Pioneers and Galileo) have added to this survey. Differentiated by orbital elements, instrument types, and capabilities, each spacecraft helped to fill blank regions of the tail's huge volume and to document its complex temporal behavior.

The IMP 8 contribution to this mapping project derives from its long orbital life and its full cross-sectional coverage in a restricted distance range (roughly 25R_E to 40R_E). In the 16 years covered by this study, 1973 to 1988, its orbit carved a 15R_E thick, geocentric spherical shell fitting within the tail's tubular boundary like a concave-convex lens. Nearly 141,000 5-min magnetic field averages fill this lens-shaped volume semiuniformly. We give here field and current maps for small and large dipole tilts and for low and high activity levels derived from IMP 8 magnetometer measurements taken inside the surveyed volume.

Full cross-sectional maps of IMP 8 are the most original contribution to tail cartography. They show the entire magnetic field pattern in the cross-sectional plane (that is, the pattern formed by the field components in that plane). The cross-tail current sheet dominates as a pronounced feature in cross-sectional maps of currents. Contour maps of the **JxB** force field outline the plasma sheet and the lobes. We also present plan (view from the top) and profile views of the tail that show the flaring and stretching of the field.

The 16 years of IMP 8 data provide a high-sample density and a reasonable degree of stationary in the representations. Unfortunately, there is no commensurate set of interplanetary magnetic field (IMF) data. Thus we were unable to bin the data according to IMF orientation. (A study of the subset of IMP 8 tail data with simultaneous IMF measurements has been completed and will be published separately.) Instead, we grouped the data into bins a low and high dipole tilt to display equinoctial symmetry and solstitial warping (especially of the current sheet) and into high *Kp*-low *Kp* bins to see whether the level of geomagnetic activity affects the patterns of the fields and currents (again, especially of the current sheet).

By creating cross-sectional, plan, and profile images of the field and cross-sectional images of the current and the magnetic force, this study graphically confirms previously inferred field, current, and plasma patterns. We present connections to prior work in the discussion section. Comparisons with quantitative magnetic field models [*Tsyganenko*, 1990] is a subject for a separate paper.

2. Data Analysis

We separated sheath data from tail data by scanning 6-hour plots of 15.36-s averages of the magnetic field. Most tail

[1]Now at Center for Space Physics, Boston University, Boston, Massachusetts.

Paper number 93JA03564.
0148-0227/94/93JA-03564$05.00

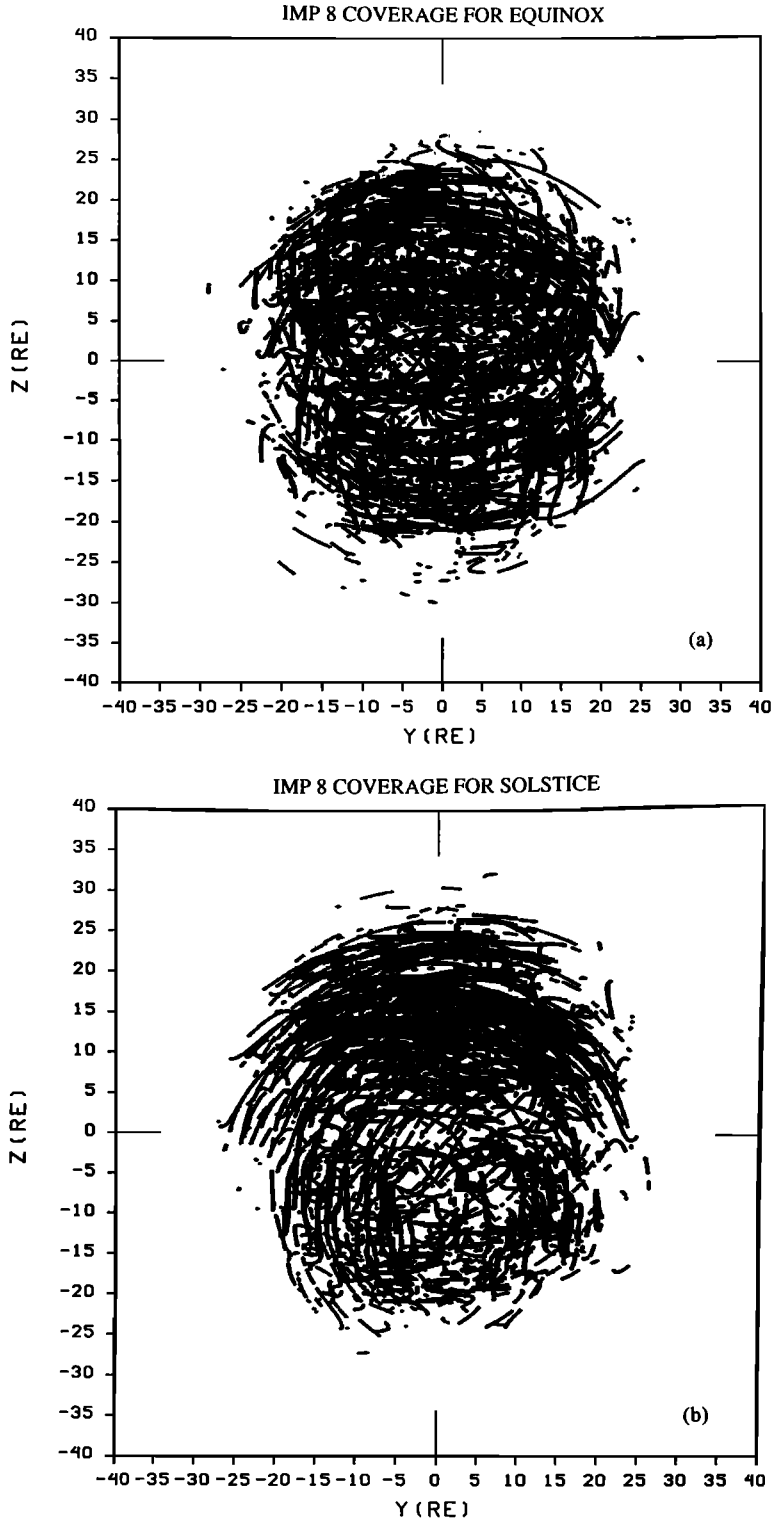

Figure 1. The IMP 8's cross-sectional coverage of the tail for (a) equinox and (b) solstice. For visual clarity, every third point of the observations is shown in both.

boundary crossings were unambiguous. The ambiguous cases affect only the near-boundary portions of the cross-sectional maps. We corrected for solar wind aberration by rotating the GSE *xy* coordinate axes 4° clockwise, then transforming to an (aberrated) GSM system [*Ohtani and Kokubun*, 1991; *Hammond et al*, 1994]. While an aberration correction has been made, for convenience we drop the "aberrated" qualifier in referring to the coordinate system in the rest of the paper. No scalings were made to account for changes in solar wind pressure or in tail flaring.

2.1. Dipole Tilt and Geomagnetic Activity (Kp) Binning

The data were separated into nearly equally populated bins of low and high dipole tilt angles, ψ, where ψ, the angle be-

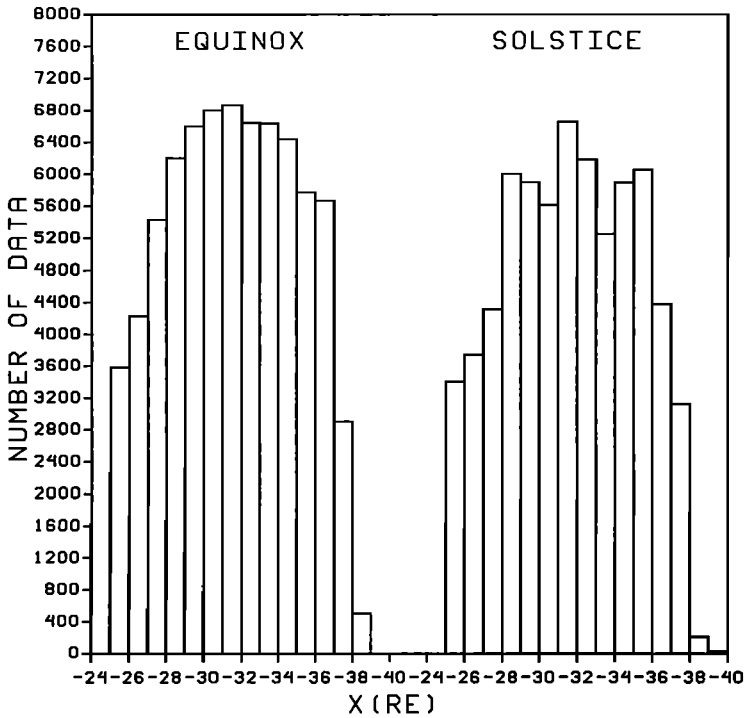

Figure 2. The histograms of the number of data points as a function of x for equinox and solstice.

tween the dipole axis and the aberrated GSM z axis, is defined to be positive in the sense of northern hemisphere summer. For high-tilt cases, negative ψ values were transformed into positive ψ values as follows: B_x --> $-B_x$, B_y --> $-B_y$, S/C_z --> $-S/C_z$, where S/C denotes the spacecraft position. This procedure doubled the number of cases in a single, high-tilt, "northern hemisphere summer" bin. On the other hand, to preserve equinoctial symmetry, no such transformation was performed for vectors in the "equinox" bin. The value of ψ that divides the data into approximately equally populated low- and high-tilt bins is 15°. Thus, for the low-tilt bin, $-15° < \psi < 15°$, and for the high-tilt bin, $\psi > 15°$, where in this case negative ψ values are folded into the positive ψ values.

The low- and high-tilt bins correspond approximately to 3-month intervals centered on equinox and solstice. They would correspond almost precisely to these intervals except that near the change of seasons the diurnal circuit of the dipole axis alternates ψ between the low- and high-tilt bins. Thus ψ binning and season binning do not exactly coincide. Despite this, the maps obtained by binning on ψ and by binning on calendar season are virtually identical. We show the ψ-binned maps here because ψ is the physically relevant parameter. Nonetheless, for ease of reference we label the bins and the maps equinox and solstice.

Figures 1a and 1b show the IMP 8 cross-sectional coverage of the tail for equinoctial and solstitial bins. They show that the spacecraft's sampling is uniform and dense in both hemispheres. For equinox the pattern is symmetric about the y and z axes. For solstice the horizontal symmetry plane is displaced toward the summer hemisphere direction. Figure 2 gives histograms of the number of data points as a function of x in the two bins. They show that the spacecraft sampled the tail more uniformly in x distance during equinoxes than during solstices, but both cases show statistically adequate sampling.

To check whether the sampling is reasonably "flat" over the tail's cross section, we determined the average x distance of all measurements inside $8R_E$ x $8R_E$ squares in the yz plane. Figure 3 gives the resulting average-x contours projected onto the yz plane for equinox. (The plot for solstice is similar.) The highest average-|x| values occur in the tail's center, while lower values occur around the edges, as expected for the IMP 8 elliptical orbit. However, the range is relatively small, about $4R_E$ from the center to the periphery. Given the relatively small change in average x over the cross section, we interpret the features revealed by the cross-sectional maps to be true cross-sectional structures. Further, we use $x = -33R_E$ to represent the average distance of the measurements.

The Kp index was used to sort the data into low- and high-activity bins. The same value of Kp was assigned to all 5-min magnetic field averages falling within the 3-hour Kp interval. For comparison with earlier studies we put the data into bins with $Kp \leq 2^+$, $Kp > 2^+$, and $Kp \geq 4^-$.

2.2. Averaging and Mapping

Cross-sectional maps were constructed by assigning magnetic field vectors (for the field maps) and current vectors (for the current maps) to each grid point of a uniform, rectangular grid of $2R_E$ spacing filling the cross-sectional plane. For field maps, each vector is an average of all measurements taken within an $8R_E$ cube centered on the grid point. Although the $8R_E$ dimension is somewhat arbitrary, it produces smooth maps. Maps based on $2R_E$ and $4R_E$ cube averages are decidedly more irregular. The coherent, large-scale structures retained in the $8R_E$-averaged maps are likely to be stable features of the tail. Averaging cubes having fewer than 10 measurements were rejected, a criterion which basically determined the shape and size of the cross-sectional pattern.

As a demonstration of the variability of the data in an averaging bin, we show in Figure 4 the standard deviation of the B_y component of the magnetic field vector normalized to its average magnitude at the each grid cube. The normalized variabil-

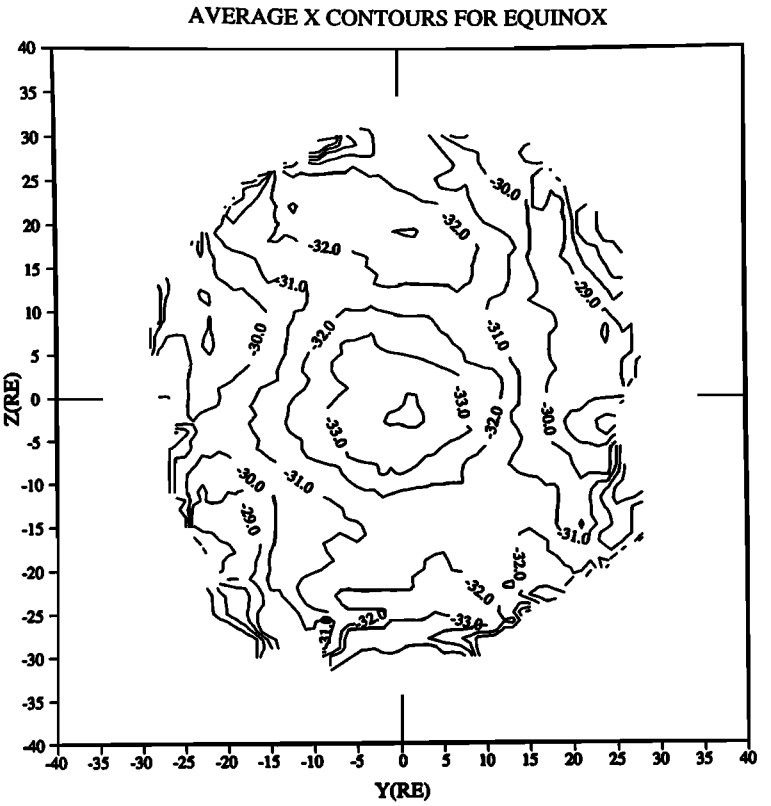

Figure 3. IMP 8 average x contours projected onto the yz plane for equinox. The difference between the highest and the lowest contour values is $4R_E$; therefore we assume the maps of this study present the tail views at $x = -33R_E$.

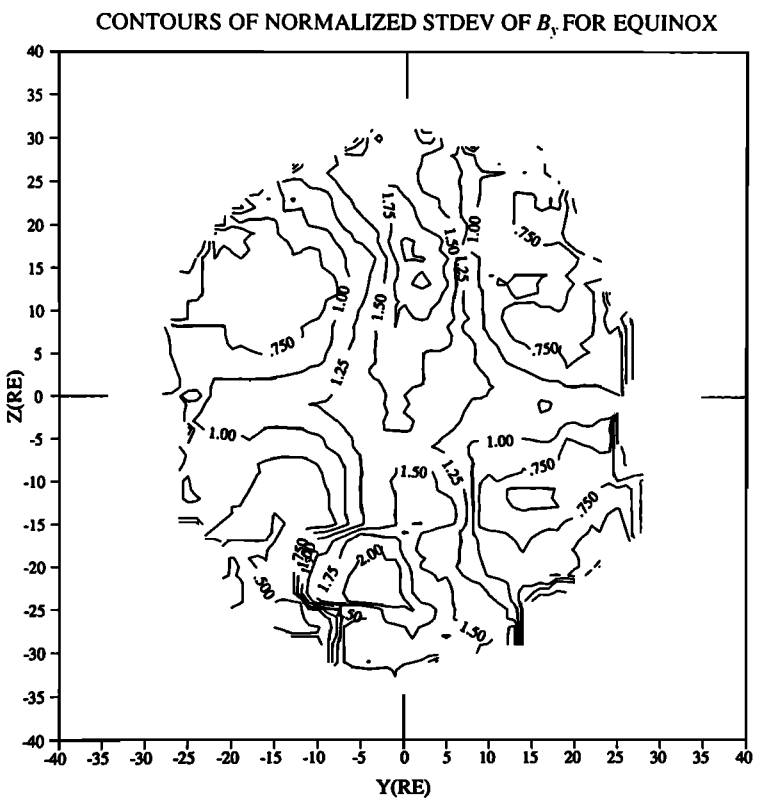

Figure 4. Contours of standard deviation of the B_y component of the magnetic field to show the variability in the B_y component. The contour values were normalized to the average magnitude of B_y.

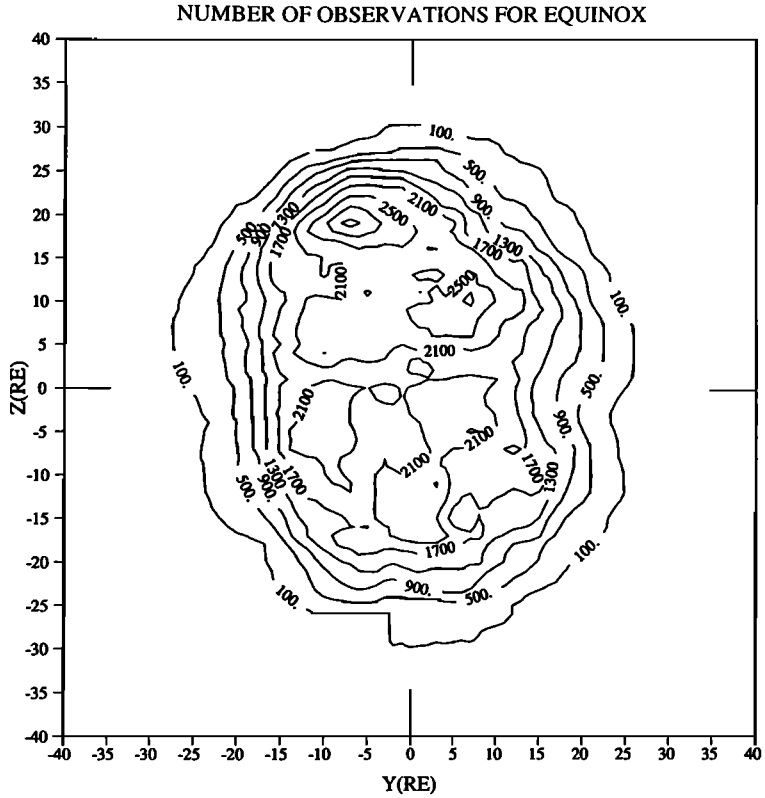

Figure 5. Contours of the number of averages used at each grid point for equinox. The field values at each grid point are an average of $8R_E$ cubes centered at that grid point. The current maps are generated from these average field values. The solstice plot is also similar to this. Contour interval is $400/(8R_E^3)$.

ity is fairly flat over the cross section. It ranges from about 0.5 to about 2. The largest values occur in the central lobes where the B_y component changes sign across the midnight meridian causing small B_y averages. Thus the maxima are artifacts of the normalization. Nonetheless, the variations are everywhere comparable to the averages. The high degree of coherence that emerges by averaging despite the variability indicates that the field has a stable, underlying order on which are superposed more or less random fluctuations of comparable amplitude.

Near the tail boundary our averaging procedure "undersmoothes" the vectors, because part of the averaging cube lies in the magnetosheath. Figure 5 gives contours of the number of averages used at each grid point for equinox. (Again, the plot for solstice is similar.) The numbers range between 2500 and 3000 over most of the central region. They drop gradually to 1000 around two thirds the way to the boundary; then they drop rapidly to 100 by the last contour. For this reason and the ambiguous boundary determinations mentioned earlier, we regard values near the boundary as suspect, especially when used to compute the current.

While cross-sectional maps were prepared for all x distances in $1R_E$ spacings from $x = -25R_E$ to $-40R_E$, we present here only the maps for the IMP 8 representative average distance, $x = -33R_E$. The features seen at this distance are present at the distances sampled.

We generated current density vectors by numerically computing the three-dimensional curl of magnetic field. In this case a cubical grid system with uniform $1R_E$ spacings was embedded within the sampled volume. A magnetic field vector was assigned to each grid point by averaging all measurements inside an $8R_E$ cube centered on the grid point. The finite difference curl of the field was then calculated at each grid point. To ensure meaningful results, especially near the boundary, we required that each of the six neighboring grid points contain at least 10 measurements. Again, while cross-sectional current maps were prepared corresponding to each field map, only maps for $x = -33R_E$ are shown. The main features are common to all distances sampled.

Besides cross-sectional maps, we present maps of magnetic field vectors on planes parallel to the equatorial plane (i.e. the xy plane) and on planes parallel to the midnight meridional plane (i.e., the xz plane).

Though a map of the tail magnetic field built by overlaying 16 years of data is about the best one can do with the present archived data sets, it is nonetheless reasonable to ask the critical question, "How well does such an average picture represent a real, self-consistent tail configuration?" Part of the answer is revealed by comparing its properties against those obtained by case studies, as we do here in the discussion section. However, there is also a simple test that if passed gives confidence that the composite picture could be an actual tail configuration. Figure 6 shows contours of the divergence of the equinox magnetic field obtained numerically in the manner described for obtaining the curl of the magnetic field. (The solstice case is similar.) The divergences are normalized by dividing by (ave B)/($2R_E$), where ave B is the average of the field magnitude in the cubes being differenced and $2R_E$ is the differencing interval. If the composite field represented an actual field, the zero contour line would encircle the boundary and

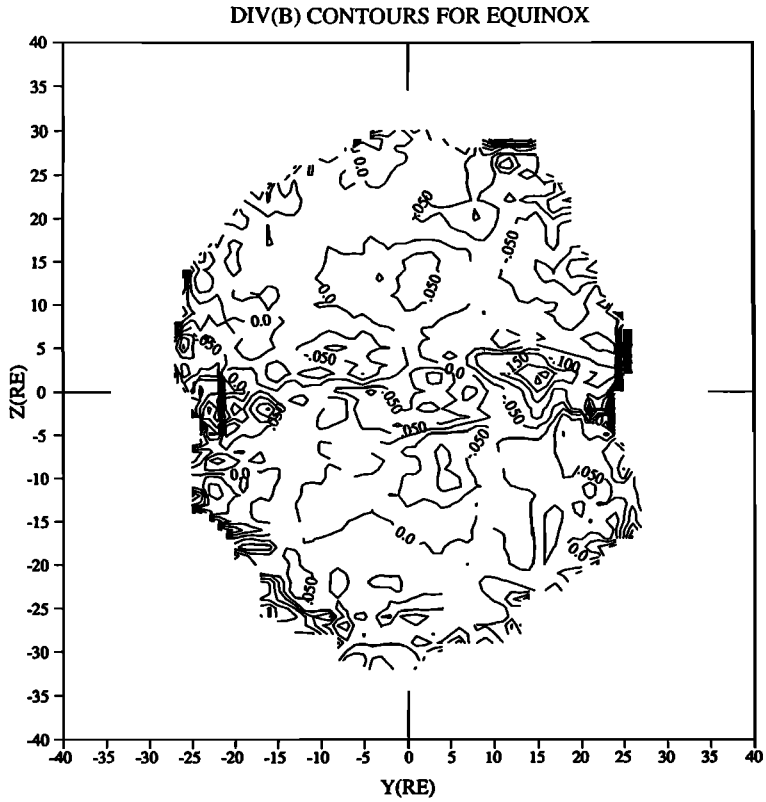

Figure 6. Contours of divergence of the magnetic field for equinox. The divergence is normalized by (ave B)/($2R_E$) as mentioned in the text.

there would be no other contours. Instead, the zero contour line is multiply connected and divides the cross section into irregular cells of positive and negative divergence. The cells are typically $10R_E$ to $20R_E$ on a "side." The typical deviation from zero in these cells is 0.05, although the normalized divergence reaches a peak of -0.2 near (y = 15, z = 0). The largest deviations from zero occur near the z = 0 line, where ave B tends to be small. On the whole, the randomness and the smallness of the deviations from zero justify treating the composite maps as approximate representations of actual configurations.

3. Results

3.1. Magnetic Field Maps

Figure 7a is a cross-sectional equinox map of the magnetic field. It shows the field components lying in the yz plane. The biggest component, B_x, is not seen in this plane (see Figure 8). The general pattern resembles iron filings on a paper sitting over the poles of a horseshoe magnet, the magnet's poles being marked in the northern and southern hemispheres by the divergence and convergence points of the vectors. These poles or nodes are $18R_E$ apart. At this x distance they define the points along the z axis that separate field lines flaring poleward from those that dip equatorward. Along the y axis, the B_z component is dominantly positive and increases from the middle toward the flanks.

The pattern is symmetric with respect to the z axis; the asymmetries that the IMF B_y is known to cause average out over this 16-year interval. (A separate paper based on IMF data deals with this asymmetry.) The pattern is also essentially symmetric with respect to the y axis, as expected for small dipole tilt angles.

Above the field nodes, the field flares outward, as expected for lobe field lines. The large radial components of the vectors near the boundary suggest magnetic field lines penetrating into the magnetosheath at the top and bottom of the figure. However, this is mostly the result of the field being nearly parallel to a flaring boundary. The pattern shows the flaring component. For example, for this data set the average flaring angle close to the boundary is nearly 15°.

Figure 7b shows two-dimensional "field lines" drawn by a standard National Center for Atmospheric Research (NCAR) graphics package based on the two-dimensional vectors of Figure 7a. Thus, these are not true projections of the actual three-dimensional magnetic field lines onto the yz plane. The field lines so constructed reveal the topology and symmetry of the two-dimensional pattern better than the vector field of Figure 7a. They also reveal the residual asymmetries and irregularities better. The figure looks odd because the graphics package does not space the streamlines in the expected way: close for strong fields and far apart for weak fields. It adds and removes field line segments to give a roughly uniform field line density.

Figures 7c and 7d are the corresponding vector and field line maps for large dipole tilts. Most noticeable in Figure 7c are the shifts of the vectors: northward in the center and southward near the flanks. The distance between the field nodes remains $18R_E$, but both are shifted about $3R_E$ northward. As Figure 7d shows more clearly, this shift is part of an arclike warping of the cross-equatorial symmetry plane. This warping will reappear in the current maps.

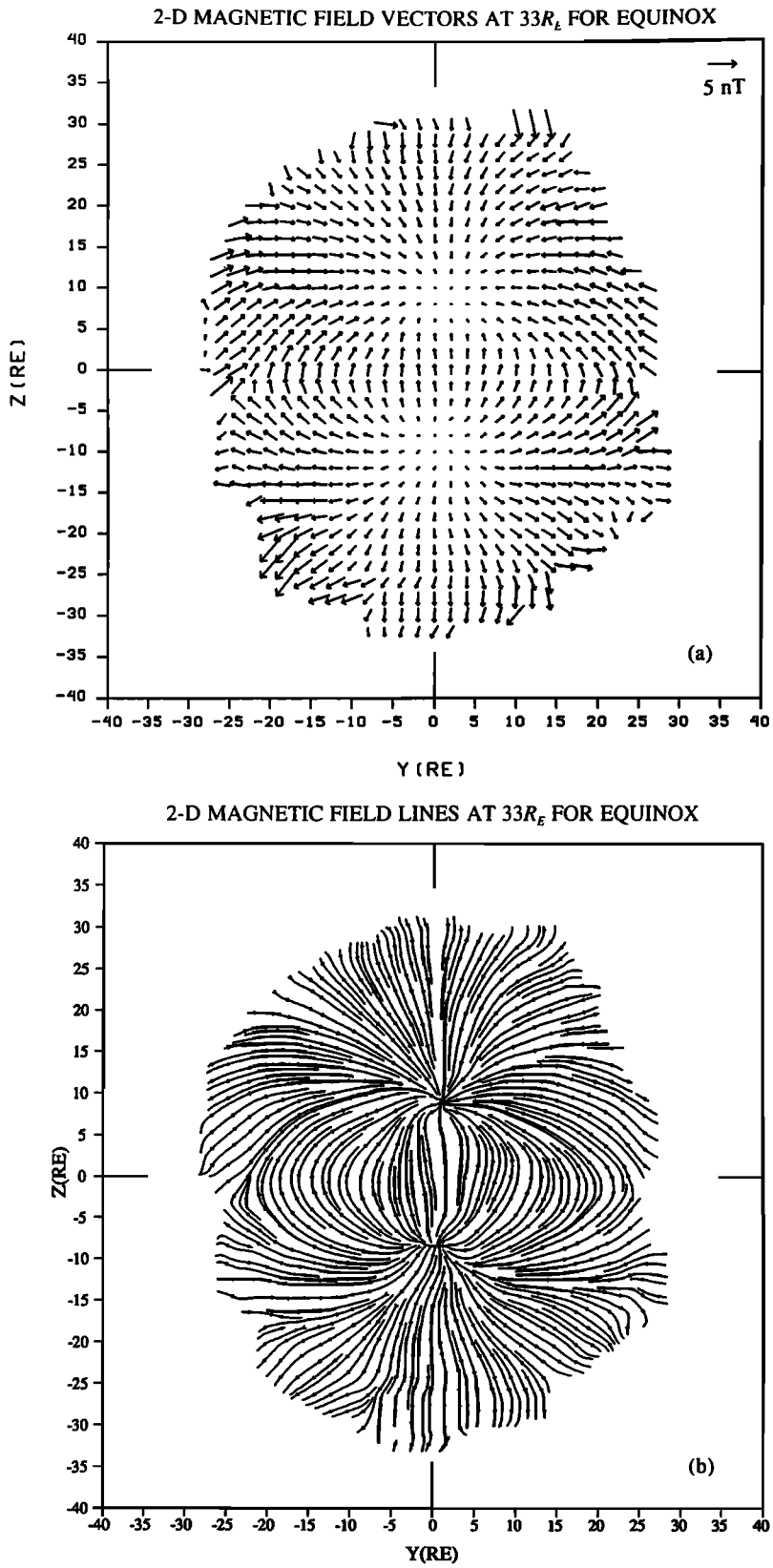

Figure 7. (a) The cross-sectional view of the magnetic field vectors at x = -33R_E for equinox. Field vectors are averaged in 8R_E cubes as explained in the text. This figure represents the flaring magnetotail at high latitudes and quite symmetrical dipolar magnetic fields at low latitudes. (b) "Field lines" drawn based on the field components (B_y and B_z) of Figure 7a. (c) Same as Figure 7a but for solstice. The dipole tilt effect is seen as an upward shift of the nodes and the vectors in the middle of the tail and downward shift of the vectors on the flanks. (d) Field lines for solstice. The archlike shape of the field lines by the tilt effect is more pronounced.

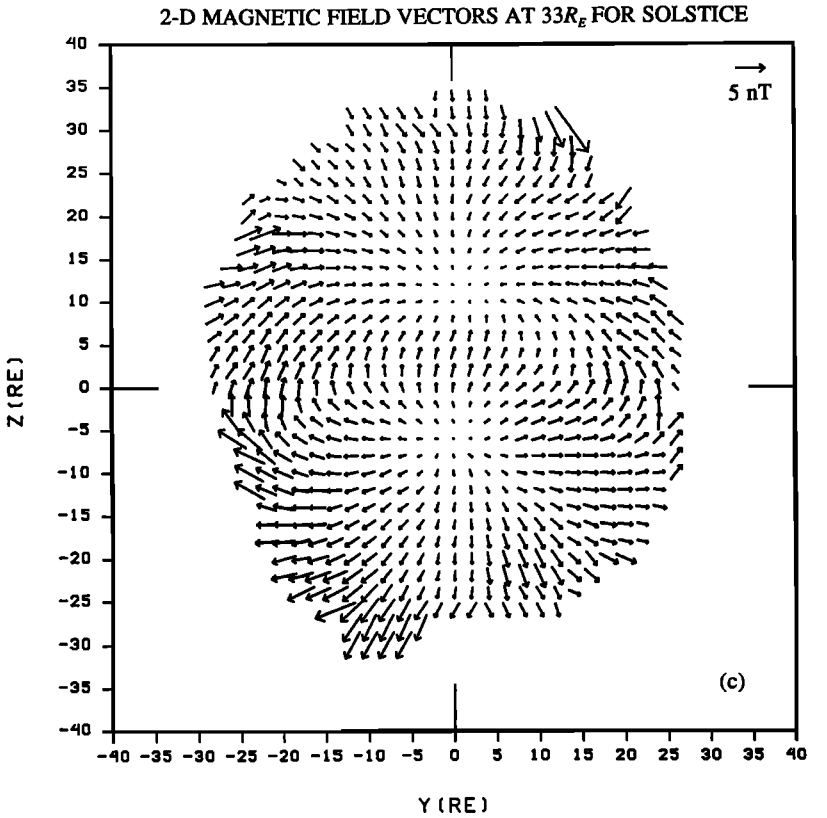

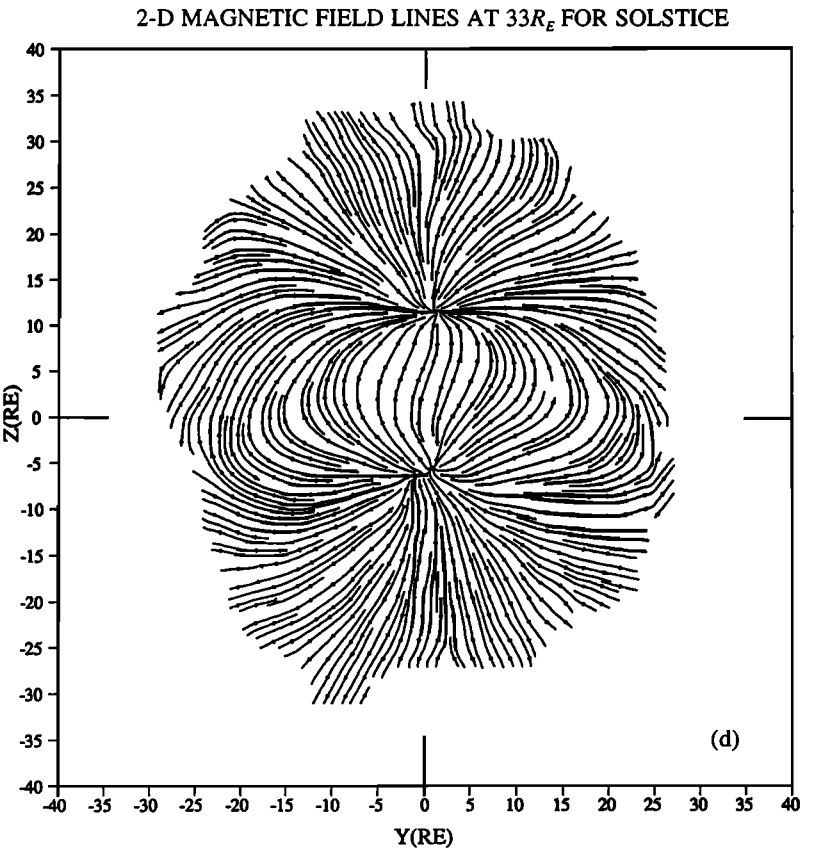

Figure 7. (continued)

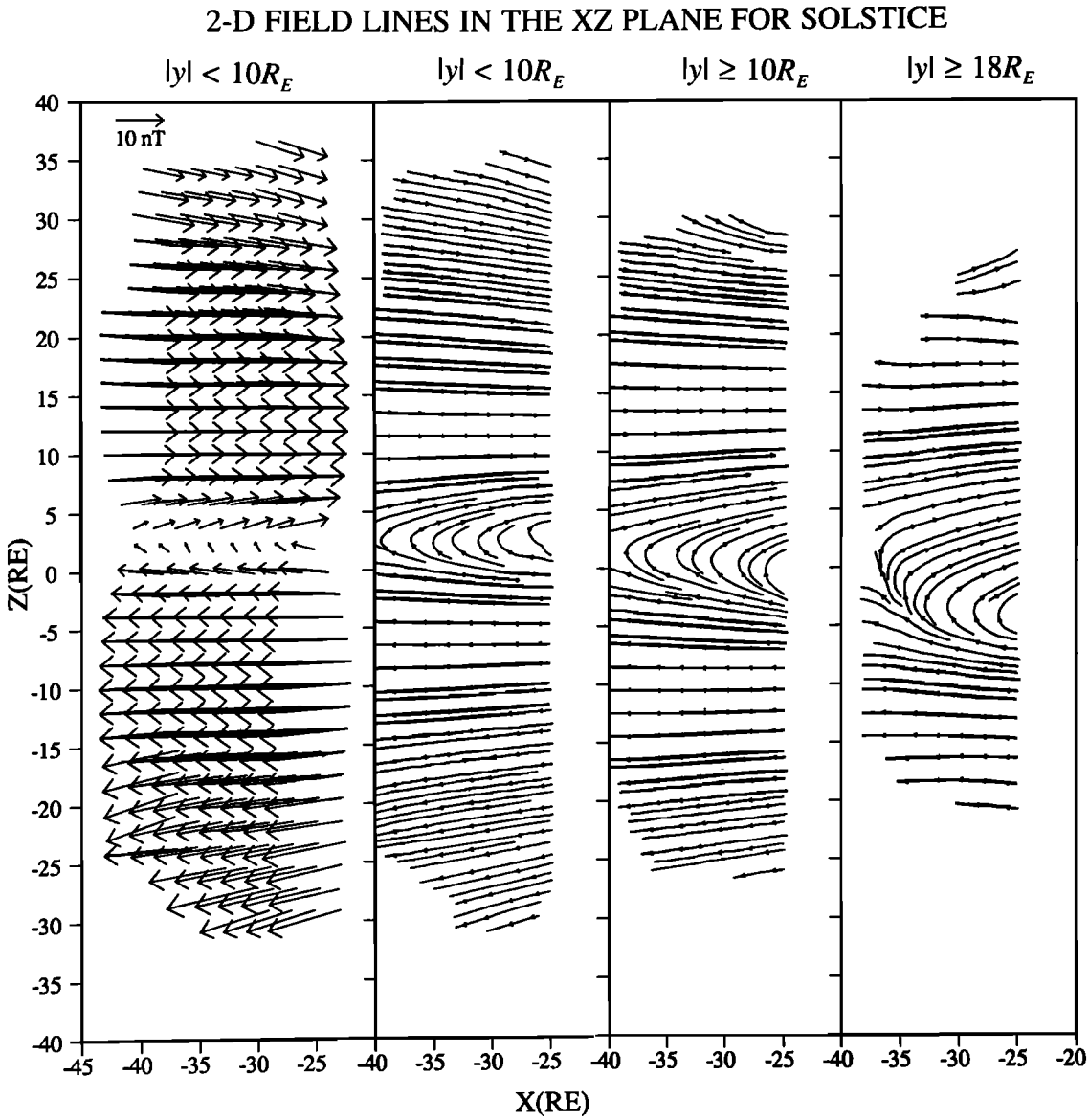

Figure 8. The composite profile maps of the magnetic field for solstice. Vectors are averaged in a (xyz) column of dimension ($8R_E$by y by $8R_E$): for (a) $|y| \leq 10R_E$, (b) $|y| > 10R_E$, and (c) $|y| > 18R_E$. Patterns demonstrate the tilt effect and the tail domains from the meridional view.

Figure 8 is a composite profile map of the magnetic field for the solstitial case. The equinoctial case is similar, but this solstitial case contains more information. The left panel shows the average xz components of the field vectors in the range $|y| < 10R_E$. The averaging here was done analogously to Figure 7: the vectors assigned to the grid points (which are separated by $2R_E$) are $8R_E$ by $8R_E$ by $20R_E$ (in the y direction) column averages centered on the grid points. The next panel shows the two-dimensional field lines based on the vectors of the first panel. The third panel is analogous to the second panel but for $|y| > 10R_E$. (The absolute value sign here means that we used both sides of the tail.) The rightmost panel continues the progression of mapping from the tail's center toward the boundary $|y| > 18R_E$.

This set of panels shows the stretching of the field lines and their reversal across a current sheet in a relatively narrow band, which from standard tail phenomenology we associate with the plasma sheet. The boundaries of the plasma sheet, however, are not evident in these maps. They appear best in contour maps of the magnetic force given in Figures 16 and 17. Tail flaring at high latitudes is apparent here. The vector panel illustrates that the field is weakest at the current sheet and strongest in the lobes. These observations are quantified in cross-sectional maps of field strength contours (Figure 15). It should be cautioned, however, that because they show long-term averages, these figures do not represent the thickness of the current sheet seen at any given time (see also the discussion of Figure 13).

In this solstitial case the midtail current sheet (first and second panels) lies about $3R_E$ above the xy plane. In the equinoctial case (not shown) the current sheet coincides with the xy plane to the resolution of the maps. The current sheets in panels 3 and 4 are displaced downward relative to the midtail current sheet. The elevation of the midtail current sheet and its progressive downward displacement toward the flanks results from the solstitial warping of the current sheet, as later cross-sectional current maps show.

In both this solstitial case and the equinoctial case, field

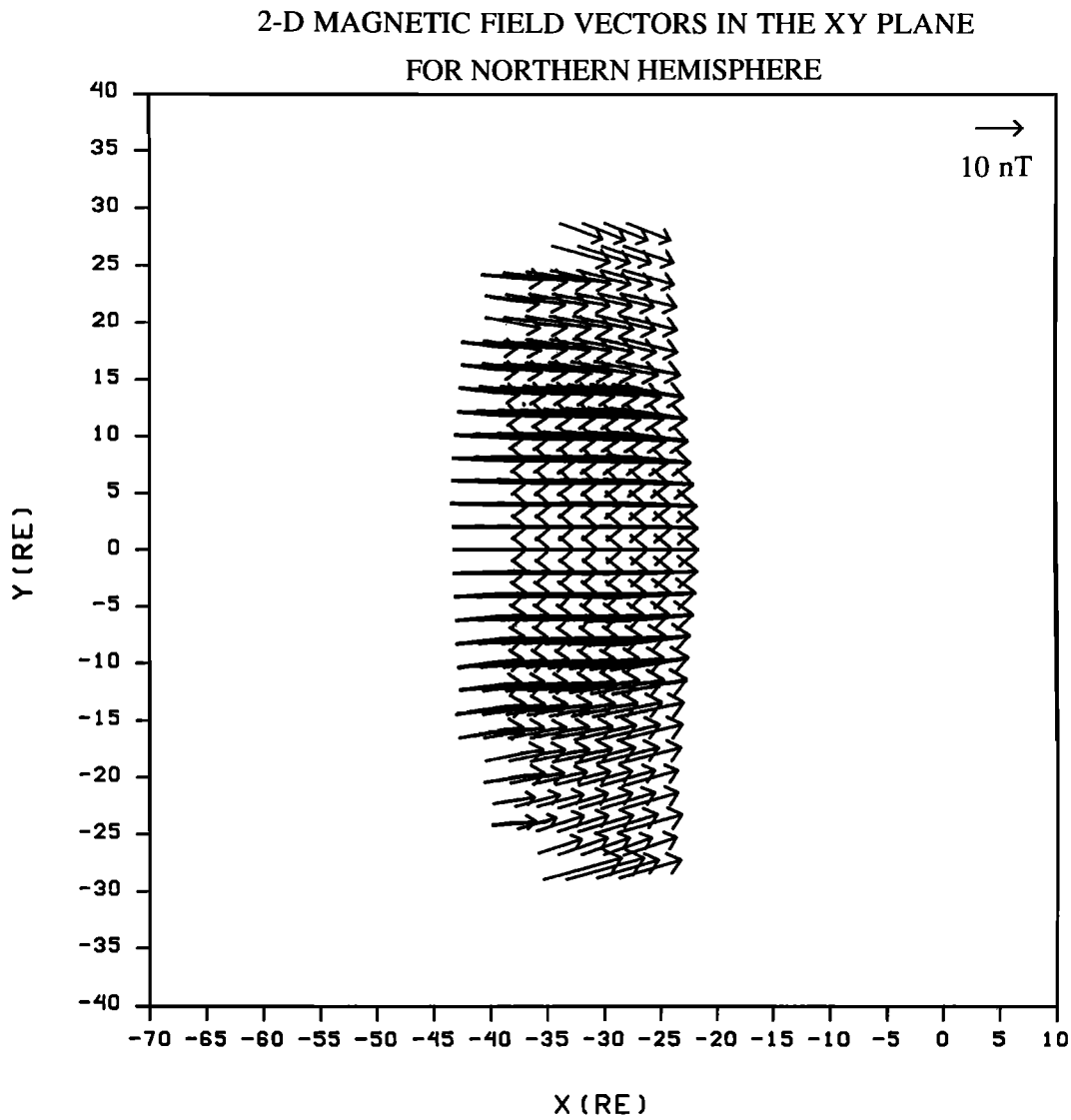

Figure 9. Plan view of the magnetic field vectors as seen from the northern hemisphere for equinox. Vectors are averages of $5R_E < z < 15R_E$ in vertical. The flaring of the magnetotail in the east-west direction is obviously seen in this map.

lines lying in the equatorial band of field reversal progress from very stretched in the middle of the tail to less stretched at the flanks (cf. panels 2 and 4). This change corresponds to the strength of the equatorial B_z increasing from midtail to the flanks. Figure 8 shows the equatorial band of field reversal thickening from the middle to the flanks. We assume that these properties are related to the bow tie shape of the plasma sheet's cross section (see the current streamline maps in the next section).

For the equinoctial case, Figure 9 shows magnetic field vectors as seen looking down onto a plane parallel to the xy plane but lying about $10R_E$ above the equator. Again, the vectors are given on a $2R_E$ by $2R_E$ grid. They are $8R_E$ by $8R_E$ by $10R_E$ column averages centered on the grid points. In this case, the columns extend from $z = 5R_E$ to $z = 15R_E$. The pattern here is rather simple: it consists of a fan of vectors pointing earthward, symmetric with respect to the x axis. As will be seen in the next section, this fan corresponds to a concave-earthward curvature of the cross-tail current sheet. The fan angle is greatest at the edges, corresponding to the flare angle of the tail's boundary. The field is strongest in the middle and weakest at the edges. The corresponding southern hemisphere map looks the same, except the arrows are reversed. Also, no new features are revealed in the solstitial case.

3.2. Electric Current Maps

This section describes electric currents obtained by numerically taking the curl of magnetic field vectors specified at each grid point in a $1R_E$ by $1R_E$ by $1R_E$, three-dimensional matrix covering the sampled volume. As before, each magnetic field vector is the average of all measurements taken in a grid-point-centered $8R_E$ cube. The current vectors are then resolved into components parallel and perpendicular to the averaged magnetic field: $J_{//} = \mathbf{J} \cdot \mathbf{B}/B$ and $J_{perp} = \mathbf{J} - J_{//}\,\mathbf{B}/B$, where B is the total field strength. Here we discuss only the perpendicular component.

Figures 10a and 10b give cross-sectional maps of current vectors and their two-dimensional current stream lines during equinox. Figures 10c and 10d show the corresponding solsti-

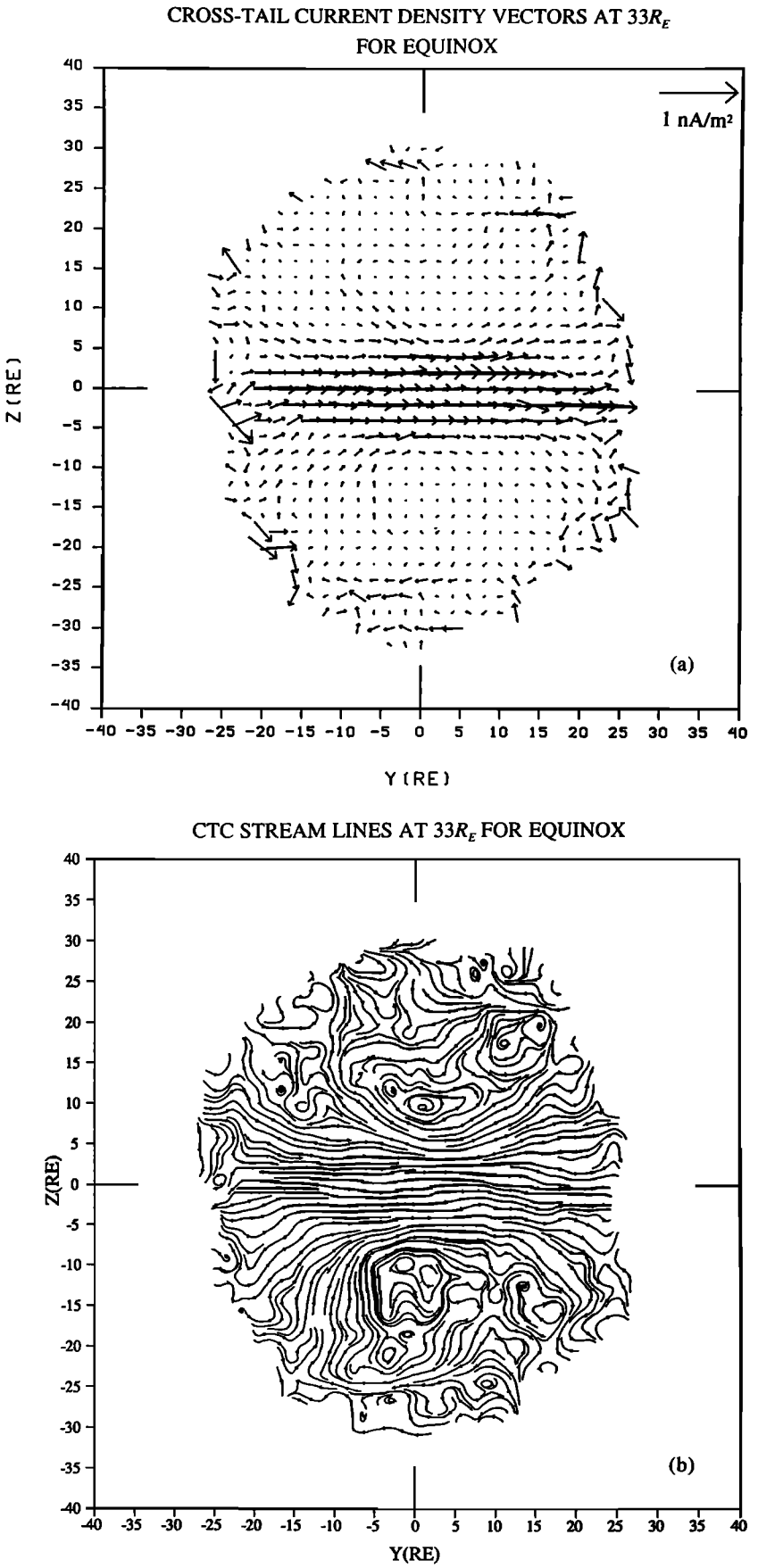

Figure 10. (a) Cross-tail current (CTC) vectors and (b) CTC stream lines for equinox at x = -33R_E. (c) Same as Figure 10a but for solstice. (d) CTC stream lines for solstice. Figures 10a-10d show the CTC shape, location, and thickness.

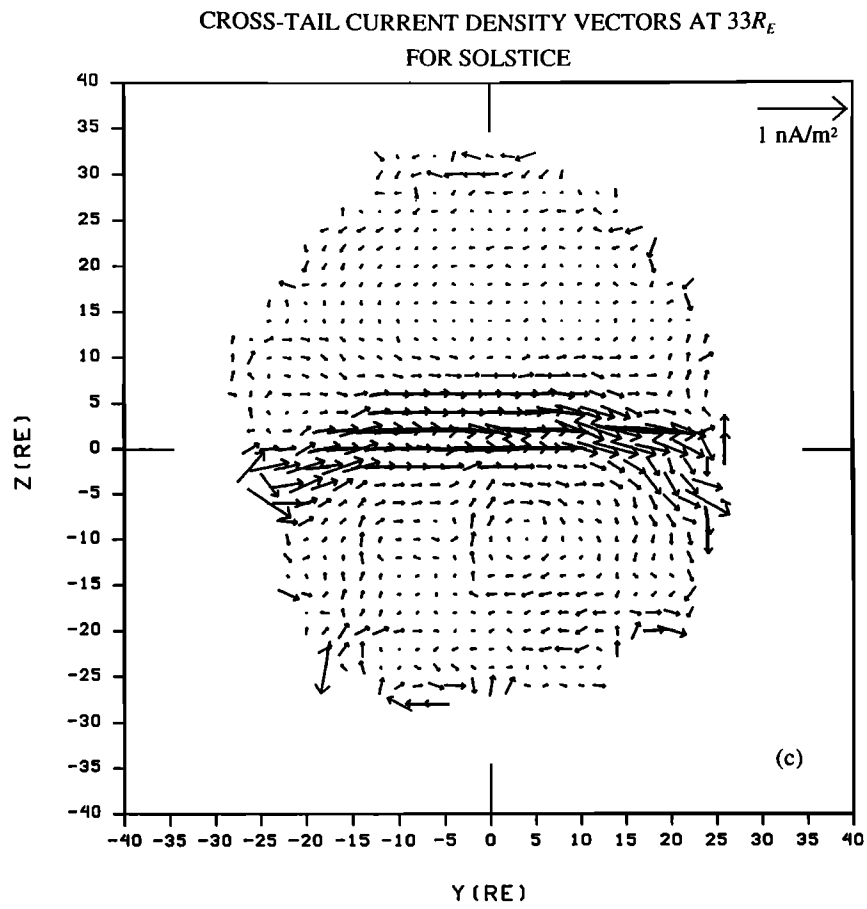

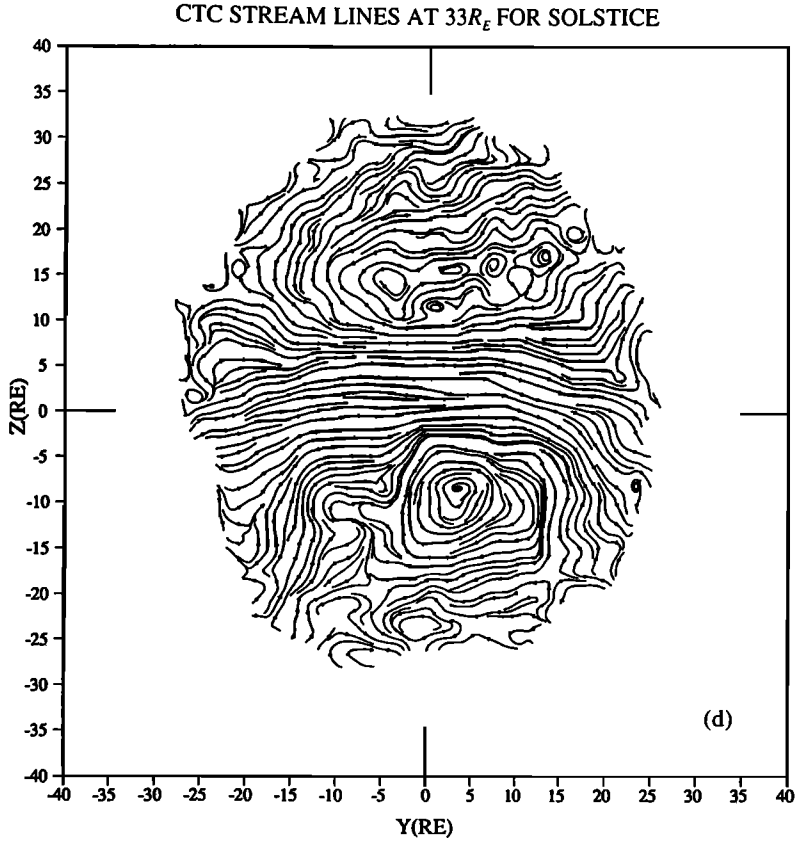

Figure 10. (continued)

tial maps. The main feature in these maps is the equatorial cross-tail current. However, the current vortices circling within the lobes also deserve notice.

In Figure 10a the equatorial cross-tail current (CTC) shows up as a quasi-uniform band of strong vectors bisecting the tail from dawn to dusk like the bar in the letter Θ. When it reaches the duskside boundary, the current should, in principle, bifurcate and return back to the dawnside by flowing along the northern and southern boundaries of the tail. Figure 10 does not allow us to check this expectation because the boundary itself, a magnetic feature produced by the return current, was intentionally excluded from this data set. We retained measurements only from inside the boundary and thus away from the return currents. Nonetheless, there is a tendency for the weak current vectors near the boundary to point in the closure direction. At the poles this tendency is somewhat more pronounced. We suspect that here we are seeing part of the closure currents flowing across the plasma mantles. Even though the mantles are boundary features, they would not have been excluded by our selection procedure.

The shape formed by the strongest vectors in Figure 10a is a thick, more or less flat bar bisecting the tail horizontally. This area does not coincide with the plasma sheet itself, which has a bow tie shape. We refer to the flat bar region of strong current as the core of the CTC. A bow tie shape is evident in the current streamlines of Figure 10b. Thus the figures together show that the core of the CTC is integrally imbedded within a much larger, geometrically well organized bow-tie-shaped current stream, which we identify with the CTC itself. The parts of the CTC that form tips of the bow tie we refer to as the wings of the CTC. Thus the CTC comprises an equatorial core of strong current vectors and four wings of weaker current vectors.

The north and south boundaries of the CTC so identified are not well defined in the figure. Along the central meridian they lie between $5R_E$ and $10R_E$ from the equatorial plane, a region where prior work places the boundaries of the plasma sheet. From there they curve away from the equatorial plane toward the flanks. They intersect the tail boundary near $z = \pm 20R_E$, but precision in pinpointing the intersections is low.

Figures 10c and 10d, showing current vectors and current streamlines, reveal the north-south asymmetry of the solstitial pattern. Figure 10c shows that the CTC core bends at solstice. If we picture a midline drawn along the core, we see that it starts at the dawn boundary below the equatorial plane, arches into the northern hemisphere, crosses the central meridian, arches symmetrically back across the equator, and ends at the dusk boundary. In its central region where its midline lies above the equatorial plane, $|y| < 14R_E$, the core is sensibly flat, as if this same central portion of the equinoctial core had simply been lifted northward about $4R_E$. (As described below, this approximate $4R_E$ distance is found by determining the central peak in the profile of current density as a function of z.) Beyond $|y|=14R_E$, the current vectors cross the GSM equator to reach the two boundaries, tracing a wide, flat arch.

The current streamlines in Figure 10d show a significantly distorted bow tie shape, corresponding to the bent core in Figure 10c. The center of the bow tie, where the knot should be, has shifted northward an appropriate amount. However, the tie's northern hemisphere wings have actually been squashed southward (pictorially speaking, no force implied),

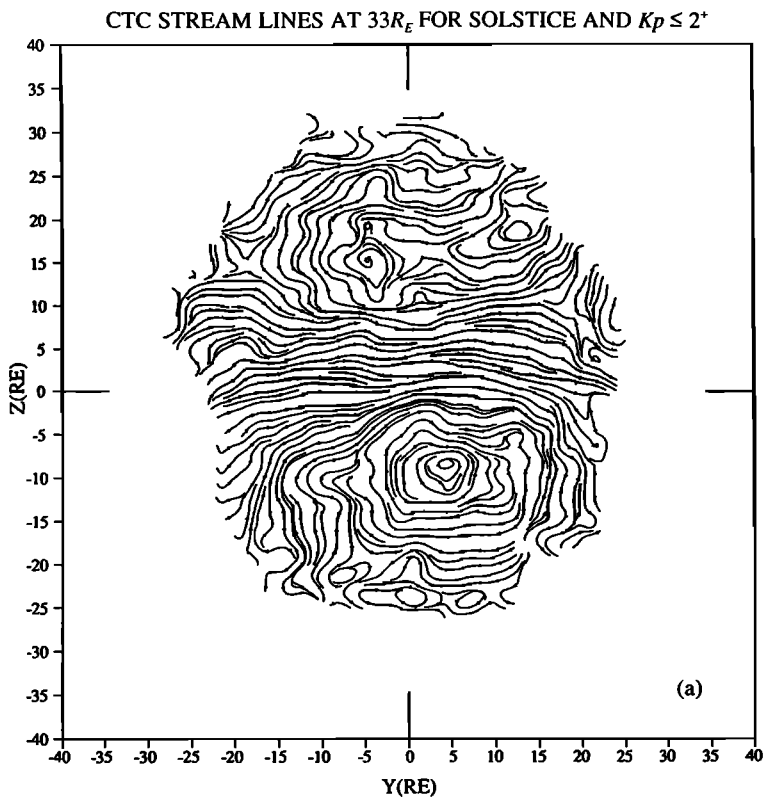

Figure 11. CTC stream lines during solstice for different geomagnetic activity levels, for (a) $Kp \leq 2^+$, (b) $Kp > 2^+$, and (c) $Kp > 4^-$.

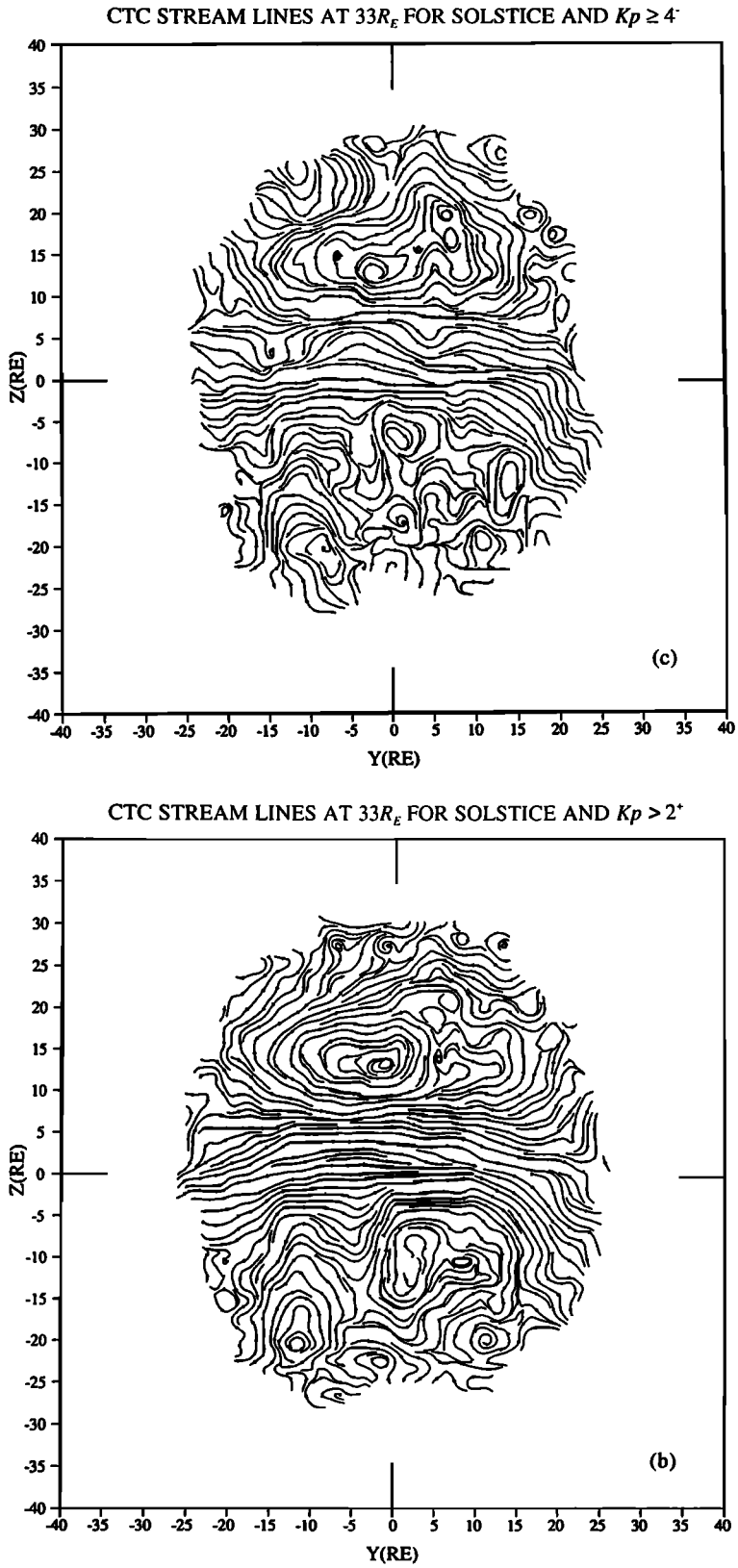

Figure 11. (continued)

so that its northern edge is rather flat. In the southern hemisphere, on the other hand, the wings have been stretched. This is more apparent on the duskside; the dawnside pattern is disrupted by a small vortex.

The lobe vortices seen in these figures are new features revealed by the ability of IMP 8 to produce cross-sectional maps. The strongest, most coherent vortex lies in the winter solstice hemisphere. This is a significant current structure. The total current circulating around it measured by the current flowing south through a plane extending straight duskward from the vortex center (from $y = 3R_E$ to $y = 24R_E$) equals one quarter the total CTC current, or half the CTC current generat-

ing the winter hemisphere lobe field. The summer solstice hemisphere vortex at this distance is replaced by an incoherent field of weak "turbulence" surrounded by a weak, coherent vortex. For the equinox case, well-defined vortices occur in both hemispheres. They have about equal strengths, but the northern hemisphere vortex is asymmetric and broad. The lobe vortices are stronger and more coherent at closer distances. Even the weak, turbulence-surrounding vortex of the summer solstice hemisphere is more dominant at closer distances.

The CTC and lobe vortices for solstice exhibit a marked *Kp* dependence. Figures 11a, 11b, and 11c show solstitial current streamlines for $Kp \leq 2^+$, $Kp > 2^+$, and $Kp \geq 4^-$. The CTC streamlines for low *Kp* are noticeably less arched than those in Figure 10d, for the whole data set, and those for the other two *Kp* levels. Nonetheless for each *Kp* level, the midline of the CTC lies between $3R_E$ and $4R_E$ above the *xy* plane along the central meridian, as it does for the average case. This position implies that the hinging distance of the current sheet does not change much with the level of magnetic activity. The winter hemisphere lobe vortex changes from highly coherent at low *Kp* to incoherent at high *Kp*. On the other hand, for the equinoctial case (not shown), the bow tie shape does not change dramatically with *Kp*, and the change in lobe coherence, while present, is also less dramatic.

Dawn-dusk asymmetry of the current patterns also persists. The current vectors in the CTC wings, representing an interior portion of the boundary closure currents, are stronger on the dusk side than on the dawn side. This holds for all distances sampled and for both "seasons" and is especially apparent in the solstice panels of Figure 10. Current vectors and streamlines in the duskside winter hemisphere are conspicuously stronger and more coherent than on the dawn side. But the same asymmetry is also evident in the equinox vector panel. The asymmetry is more noticeable at closer distances.

The first panel in Figure 12 gives a plan view of CTC vectors for equinox. The vectors are "vertical" averages through the main part of the CTC ($-5R_E < z < 5R_E$) of the current vectors at each grid point. The figure projects these averages onto the *xy* plane. The vectors fill the area defined by the outermost distance that the spacecraft can reach and $x = -25R_E$. They are dominantly in the *y* direction with a curvature toward the Earth. That they are weaker at the edges shows the divergence of the current out of the core and into the wings.

The second panel in Figure 12 shows the corresponding current streamlines. They are concave earthward, with the great-

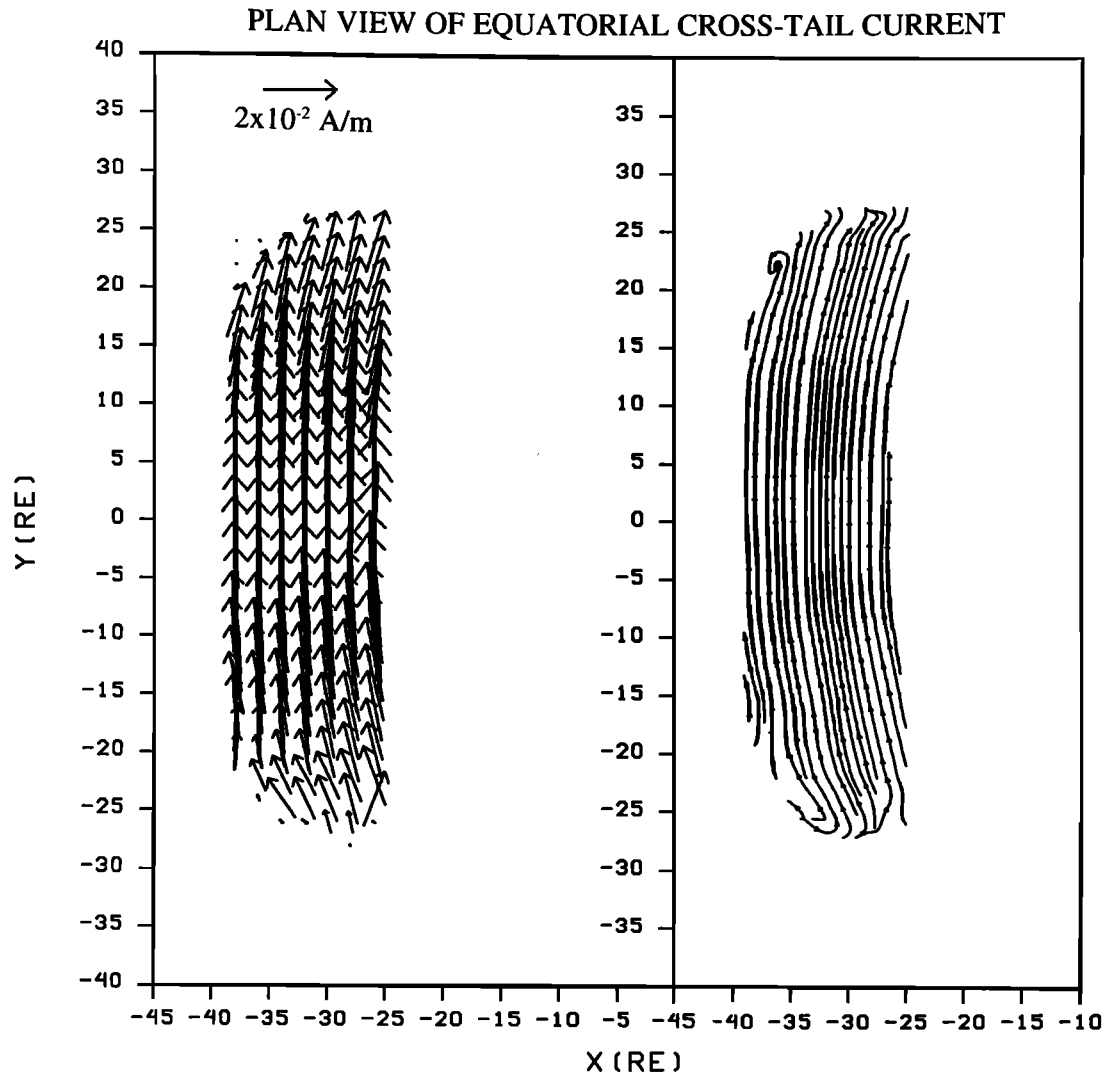

Figure 12. Plan view of the CTC vectors and current stream lines for equinox. Vectors are vertical averages of Figure 10a over the range $|z| \leq 5R_E$.

est curvature close to the boundaries. Their average radius of curvature is approximately $80R_E$. Note that this is more than twice the distance to the Earth. We may therefore infer that the radius of curvature in the equatorial plane of the equatorial current increases with distance from the earth, from the ring current to the CTC, faster than the distance to the earth itself. For the ring current the radius of curvature essentially equals the distance to earth, as the name implies. However, we see here that for the CTC between $25R_E$ and $40R_E$, it exceeds twice the distance to earth. The radius of curvature of the CTC also increases with *Kp*, from $70R_E$ for $Kp \leq 2^+$ to $95R_E$ for $Kp > 2^+$.

To study the profile of current density along the central meridian, we increased the resolution in the *z* direction by recomputing the current based on magnetic field averages in $8R_E$ by $8R_E$ by $1R_E$ *xyz* slabs instead of $8R_E$ cubes, as before. To recover some of the lost benefit of averaging in *z*, we averaged the current vectors in the *y* direction over the range $-5R_E$ to $+5R_E$. Since parameters change slowly in the *y* direction in the tail's middle, this means of averaging should not affect resolution in the *z* direction.

Figures 13a and 13b for equinox shows central meridian profiles of the current density and B_x, the component of the field most directly related to the current. The dark lines are averages, and the light lines are one standard deviation envelopes. The current profile has a prominent, narrow central peak flanked by shoulders and other, subsidiary peaks. The full width at half maximum of the central peaks is close to $3R_E$. Its peak value is approximately 0.9 nA/m^2. The locations of the peak and the $B_x = 0$ point lie about $1R_E$ below the equator. This must be taken as a measure of the inaccuracy in fixing these locations by this method. In the B_x profile the shoulders and subsidiary peaks correspond to relatively inconspicuous inflections. For comparison, Figure 13b shows a Harris sheet profile [*Harris*, 1962]

$$B_x = B_0 \tanh (z/z_0)$$

with the parameters $B_0 = 17.6$ nT and $z_0 = 3.5R_E$. This gives a thickness for the current carrying region (presumably the plasma sheet) of $7R_E$.

Figures 13c and 13d show the corresponding profiles for solstice. The central current sheet is squatter, displaced, and asymmetric. The value of the central peak is 0.6 nA/m^2. Its median line lies about $3R_E$ above the equator. Its summer hemisphere border is narrower than its winter hemisphere border. The same Harris sheet profile is shown here displace $3R_E$ toward the summer hemisphere.

The actual thickness of the central current sheet must typically be less than the $3R_E$ values found here. This upper limit on the typical current sheet thickness averages the field over 16 years, including all solar wind flow directions, and over $1R_E$ in the *z* direction. Nonetheless, considering that a relatively thin current sheet ($3R_E$) survives such heavy averaging, it would seem to follow that a thin, central current sheet typifies the tail between $25R_E$ and $40R_E$, despite disruptions attending substorms.

3.3. Field and Force Contour Maps

This section emphasizes the tail's dynamics rather than structure. It shows where the magnetic field and the magnetic force are strong and weak. Magnetic force here means **JxB**, which is computed using the $8R_E$ field averages and their curls. Maps were computed for two components of the force: the *x* component and the component in the *yz* plane. The *x* component of the magnetic force balances the *x* component of the pressure gradient and so is greatest in the plasma sheet. Thus, $(\mathbf{JxB})_x$ contours outline the plasma sheet. The *yz* component balances the *yz* component of the pressure gradient and so is greatest on the boundaries of the plasma sheet. Thus the peak of the $|\mathbf{JxB}|_{yz}$ contours crudely defines the plasma sheet boundary. Again we must caution that since both $(\mathbf{JxB})_x$ and $|\mathbf{JxB}|_{yz}$ maps are long-term averages in $8R_E$ cubes, the effects of spatial/temporal averaging must be kept in mind in relating the features revealed in these maps to case studies.

Figure 14 shows field strength contours for the equinox data. Thought of as a two-dimensional pattern, it shows an equatorial bar where the strong current core flows, bow tie wings, and closed contours corresponding to the lobe current vortices. Thought of instead as a topographical map, it depicts two broad hills rising out of the page separated by a narrow deep valley sinking into the page. The hills correspond to the northern and southern lobes. Their peaks align approximately with the central meridian, close to $10R_E$ above and below the equatorial plane. That the peaks lie so close to the equatorial plane shows that the current throughout most of the lobes flows from dusk to dawn, opposite to the flow in the CTC. The hills top out at 18 and 19 nT. (The 1-nT difference between the heights of the peaks might not be statistically significant, for the error in determining the mean is 0.8 nT.) The intervening valley running along the equatorial plane corresponds to the plasma sheet. The field strength drops to 2 nT in the heart of the valley.

The depth of the valley (2 nT) reflects the field strength at the center of the current sheet or the value of B_z at the place where B_x changes sign. We resolved this small region of low field strength against a background of high B_x by first averaging the field components in the $8R_E$ averaging cubes, then finding vector magnitude of these component averages. We chose this method over the more usual averaging of field strength precisely because it resolves the valley's depth ($+B_x$ and $-B_x$ components cancel in the cubes straddling the neutral sheet). However, it exaggerates the valley's width. Since like the peaks, the valley is a major topographical feature of the tail, we put greater emphasis on its depth.

Comparing maps for $Kp \leq 2^+$, $Kp > 2^+$, and $Kp \geq 4^-$ with Figure 14 shows very little difference in the sizes and shapes of the equatorial core, the flanking wings, and the lobe vortices. However, the topographical parameters change; the depth of the valley stays at 2 nT, but the tops of the peaks vary from 17 nT for the low-*Kp* map to 21 to 22 nT for the high-*Kp* map, an increase of roughly 25%. For the solstice all-*Kp* case (not shown), the valley shifts northward in the middle and southward at the flanks, like the midline of the CTC core in Figure 10c. The deepest parts again reach 2 nT. The summer hemisphere hill is very broad, almost like a mesa. Nearly 25% of its area lies at an altitude above 16 nT, the last contour. The winter hemisphere, by contrast, is quite peaked. In less than 25% of its area, contours rise from 17 nT to over 20 nT. The 3-nT difference in the heights of the hills exceeds the 0.8 nT error in determining the mean and is much bigger than the noise in the data as indicated by contour irregularities. Thus the stronger lobe field in the winter hemisphere appears to be a real solstitial property. The contours in both hemispheres are systematically shifted to the duskside. For example, the winter hemisphere peak lies at $y = 4R_E$. This is

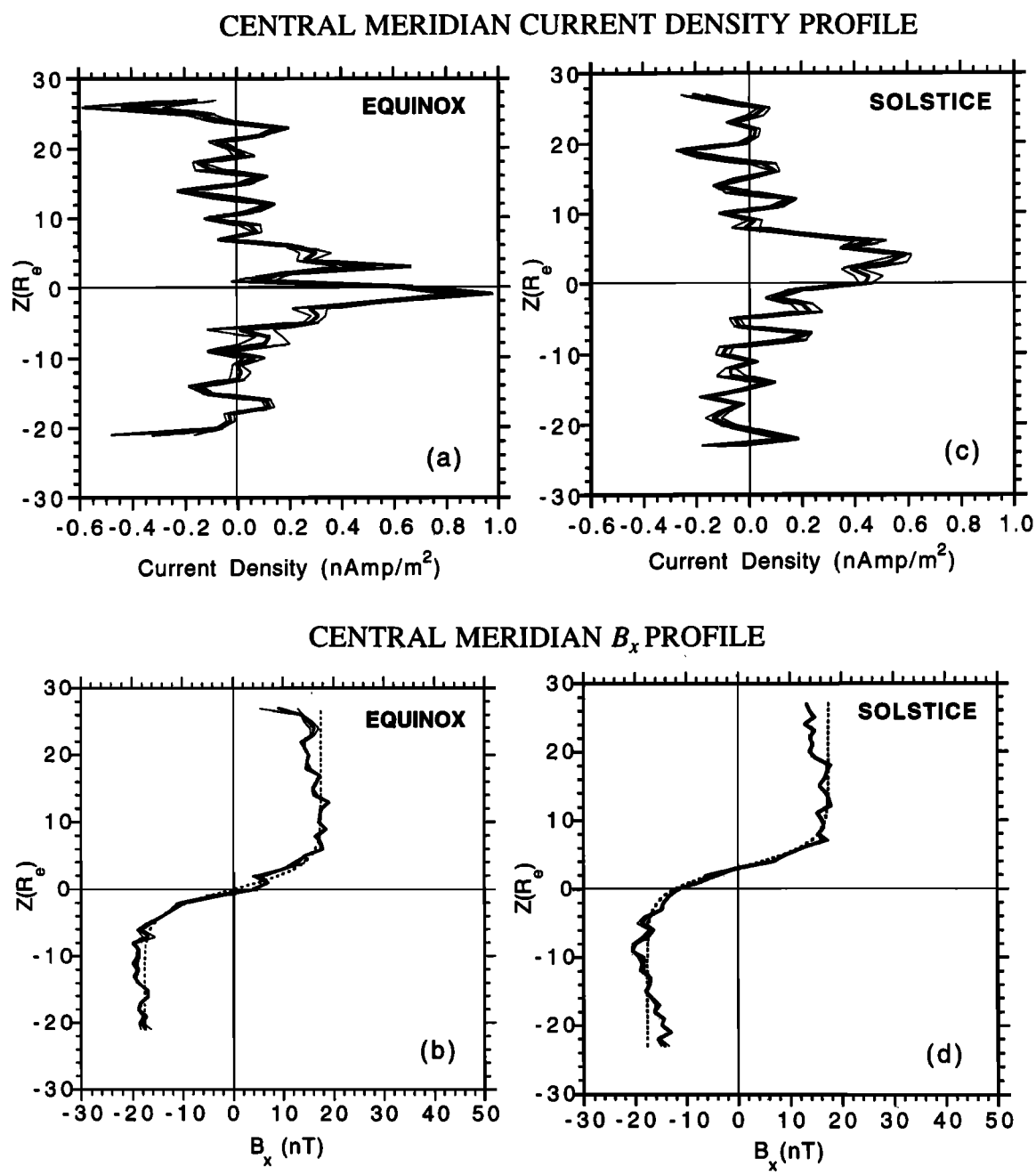

Figure 13. Central meridian current density and B_x profiles for (a) and (b) equinox, and (c) and (d) solstice. The figure is based on the magnetic field vectors averaged in $8R_E$ by $10R_E$ by $1R_E$ (x, y, z) slabs instead in $8R_E$ cubes as in Figures 7a and 7c.

another instance of the dawn-dusk asymmetry noted in reference to Figure 10.

Figure 15 shows contours of the x component of **JxB** for equinox. Its most notable feature is the equatorial bar having nearly the same size, shape, and position as the CTC core in Figure 10a, and the equatorial field strength valley of Figure 14. This feature reinforces the impression that the CTC actually has distinct parts: a core and wings. Despite breaking up into three, large contour islands (one located near the northern margin of the bar's eveningside and two dominating the midline of the flanks) the x component of the force is strong and fairly uniform over most of the bar's width. The case is better made with the solstice map (not shown) where the three islands, while distinctly present, do not interrupt the flow of the contours from dawn to dusk. The margins of close contour spacings at the bar's borders most likely define the boundaries of the plasma sheet.

Figure 16 shows contour maps of the strength of the yz component of the **JxB** force for the equinoctial case. The two pronounced contour islands near the middle of the figure evidently mark the central portions of the northern and southern borders of the plasma sheet. This inference is supported by the fact the centers of the islands fall on the margins identified in Figure 15 as the plasma sheet boundaries. The duskward displacements of the islands again points to a persistent dawn-dusk asymmetry in the structure or dynamics of the plasma

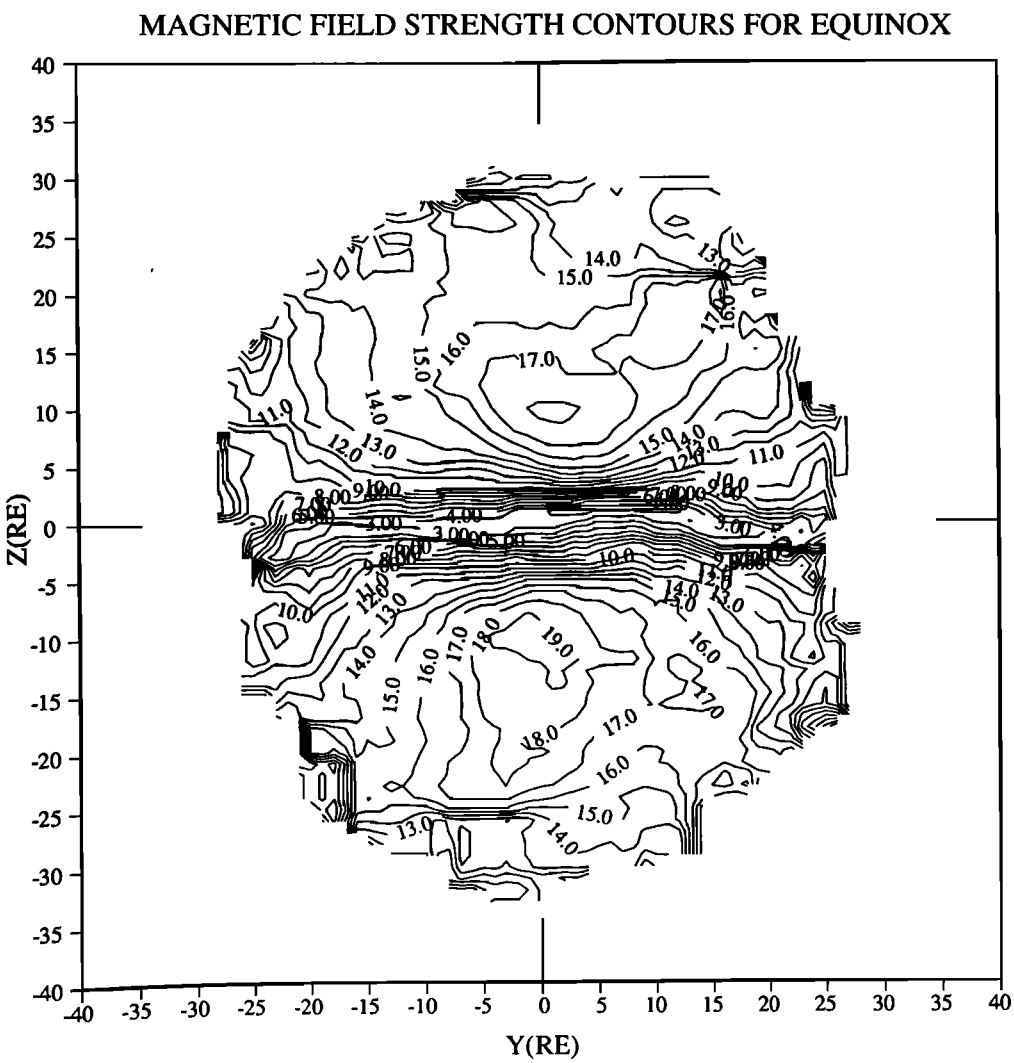

Figure 14. Magnetic field strength contours for equinox.

sheet. The rest of the plasma sheet's borders can be traced through contour islands and peninsulas running east and west from the main islands. Nonetheless, the concentration of the magnetic force to the center of the tail is the salient aspect of the figure. Toward the flanks the boundary of the plasma sheet seems to loose its definition in this parameter. For the solstice cases (not shown) the steepest contours and largest islands occur on the winter (southern) edges of the plasma sheet. The dawn-dusk asymmetry is again apparent.

If we use the north-south distance between the centers of the islands defining the north and south borders of the plasma sheet in Figure 16 to measure the thickness of the plasma sheet, we find $7R_E$ for the equinox case and $6R_E$ for the solstice case. These are presumably upper limits on the typical thickness because of the long time averaging.

4. Discussion

The maps of the last section show many previously reported features and properties of tail structure. However, some aspects are seen here for the first time full cross section. There are also new features. Here we discuss some of the old and new features and relate them to prior work in the order of Figures 7 through 16.

Regarding Figure 7 (the cross-sectional view of magnetic field vectors and field lines for equinox and solstice) *Fairfield* [1979] also reported dipolelike fields near the flanks of the tail. He showed that the B_z component is twice as large there as in the center. Consequently, he concluded that the plasma sheet is twice as thick on the flanks as in the center. *Bame* [1967] and *Behannon* [1970] also noted the thickening of the plasma sheet toward the flanks. This is the plasma sheet's bow-tie shape. *Fairfield* [1979] also observed that positive B_z values occur below $z = 9R_E$ from the midplane, and negative values occur above $z = 9R_E$ as a result of the fields flaring away from the xy plane. At the tail's center, the magnitude of the B_z component is about 2 nT; this is about the same as *Fairfield*'s [1979] midnight sector value.

Figures 7a and 7b display the full cross-sectional geometry of these features. Figures 7c and 7d show that during solstice the dipolar pattern is distorted by lifting it in the middle and pulling it down at the flanks. This distortion has not been explicitly noted before, although it is related to the well-known arching of the plasma sheet during solstice (see below).

There is a natural, subjective tendency to identify the nodes with the borders of the plasma sheet. They seem to divide the tail into closed field line (i.e., plasma sheet) and open field line (i.e., lobe) regions. Indeed, one early MHD equilibrium

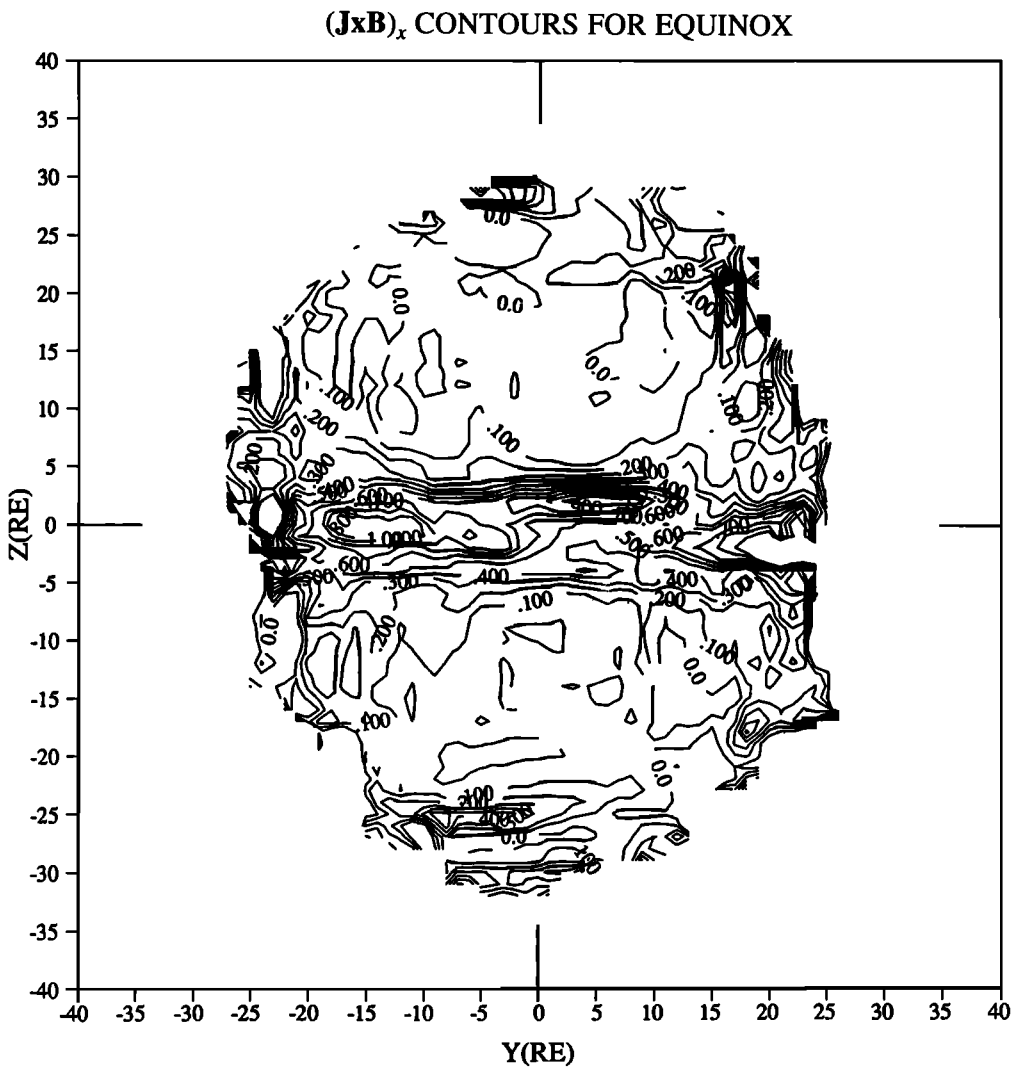

Figure 15. (JxB)$_x$ contours for equinox. The contour values are multiplied by 10^{-18} to get magnetic force in (N/m^3).

model of the tail used the condition of the field lying parallel to the tail axis to mark where the thermal pressure in the plasma sheet balances the pressure in the lobes, and thus, to mark the plasma sheet boundary [*Voigt and Hilmer*, 1987]. This is a false impression, however, as the discussion of Figure 15 shows. It gives the averaged plasma sheet thickness as $7R_E$ compared to the $18R_E$ separation of the nodes. This indicates the lobe field lines equatorward the nodes converge toward the equator at this distance before they turn and flare poleward. As a corollary the boundary of the plasma sheet lies on converging field lines, as in models with a distant neutral line. Figure 17 is drawn to illustrate these points.

Figure 8 gives profile views of solstitial field line geometry showing the so-called neutral surface at different y distances. *Ness* [1965] first reported that a neutral surface equatorially bisects the tail and separates the oppositely directed field lines of its northern and southern lobes. He noted that this surface is a permanent feature of the tail; indeed it is the sine qua non of the tail. In Figure 8 the neutral sheet appears as a thin, weak magnetic field region, squeezed between stretched, x directed field lines. The magnitude of the B_z component at the "neutral" surface measures the dipolarity of the field [*Speiser and Ness*, 1967; *Fairfield*, 1979; *McPherron*, 1991]. The most dipolar field lines are furthest from the midnight meridian illustrating the plasma sheet's thickening toward the flanks. The downward progression of the neutral sheet from the tail's center in this solstitial case corresponds to the lifting of the nodes and the dipping of the flanks in Figures 7c and 7d.

Figure 9 shows the fanlike flaring of the magnetic field in the xy plane for the equinox case. Figure 18 gives the flaring angle, $\alpha = \tan^{-1}(B_y/B_x)$, calculated from Figure 9. A linear, least squares fit to these data gives α(deg) = (-0.656 ± 0.005)$y(R_E)$ + (0.762 ± 0.078). Using unaberrated IMP 6 measurements, *Fairfield* [1979] finds α = -0.9y - 1.7. Fairfield's larger flaring coefficient probably reflects the fact that his average x distance is $27R_E$ whereas ours is $33R_E$, and flaring decreases with distance. The constant term in these fits should be zero in a properly aberrated coordinate system. A 3° aberration angle removes the constant term in Fairfield's fit. The fit to our data shows that they are aberrated 1° too far. This makes the actual aberration 3°, which agrees with Fairfield. Evidently, the standard 4° aberration angle should be revised to 3°.

Figures 10a and 10b, giving equinox current vectors and stream lines, show that the cross-tail current has distinct core and wing parts. The core contains most of the cross-tail cur-

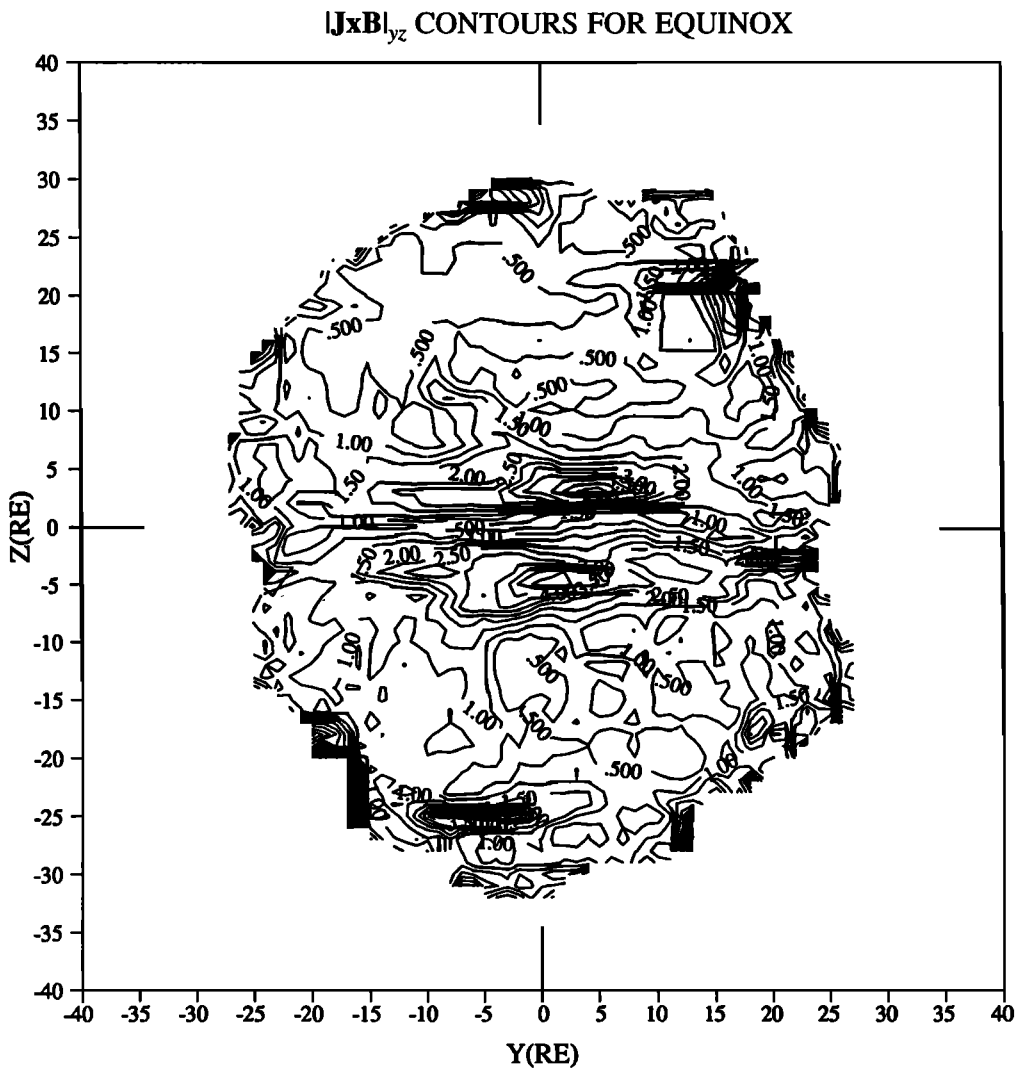

Figure 16. $|\mathbf{JxB}|_{yz}$ contours for equinox. The contour values are multiplied by 10^{-18} to get magnetic force in (N/m^3).

rent in the center, but the wings carry much current at the flanks. No corresponding dual structure has been reported in the plasma data from the plasma sheet. The dual structure persists for solstice but with distortions, as Figures 10c and 10d show.

Current sheet geometry has been investigated by many authors and understanding of it has increased as data have accumulated. At first it was understood that, for high dipole tilt angles, the current sheet lies parallel to the equatorial plane of GSM [*Ness*, 1965] and is simply displaced from that plane like a flat rectangular surface [*Murayama*, 1966]. Later, it was realized that a curved surface better defines the shape of the neutral sheet. *Russell and Brody* [1967] represented it by a circular surface above the equator. *Fairfield and Ness* [1970] extended the circular surface to an ellipse. It is now known that the current sheet not only rises above the equatorial plane in the tail's middle but also crosses and drops below it on the tail flanks [*Fairfield*, 1980]. Fairfield modeled its shape with a displaced ellipse. Other statistical and modeling studies subsequently dealt with determining its shape and location. However they show more or less the same effect with different data sets and at different tail distances [e.g., *Gosling et al.*, 1986; *Dandouras*, 1988; *Hammond et al.*, 1994; *Voigt, 1984*; *Tsyganenko, 1989*; *Walker et al.*, 1989]. For example, *Hammond et al.* [1994] compare their results with different neutral sheet models and find that for high dipole tilt angles, their neutral sheet has the basic displaced elliptical shape of the Fairfield model rather than flattening near the flanks as suggested by the *Murayama* [1966] and *Dandouras* [1988] models. Near the flanks their neutral sheet is very close to the Fairfield model, but in fact curves slightly more. They give a more precise formula for the shape.

Figures 10c and 10d show this much discussed warping for the whole CTC as it arcs above the z=0 plane in the middle and dips below it on the flanks. This arclike shape is more pronounced in the magnetic field lines of Figure 7d. Quantitatively, the core of the CTC rises by about $4R_E$ above the z=0 plane in the middle and dips $7R_E$ below it at the flanks. The northern part of the wings become flatter, while their southern parts are more stretched. This aspect of the solstitial distortion has not been noted previously.

The main points extracted from Figure 10 are summarized in the sketches in Figure 19. Figures 19a and 19b give the CTC structure for equinox and solstice. A strong, central band of current (the CTC core) lies sandwiched between weak, periferal splays of current (the CTC wings) like the body and wings of a

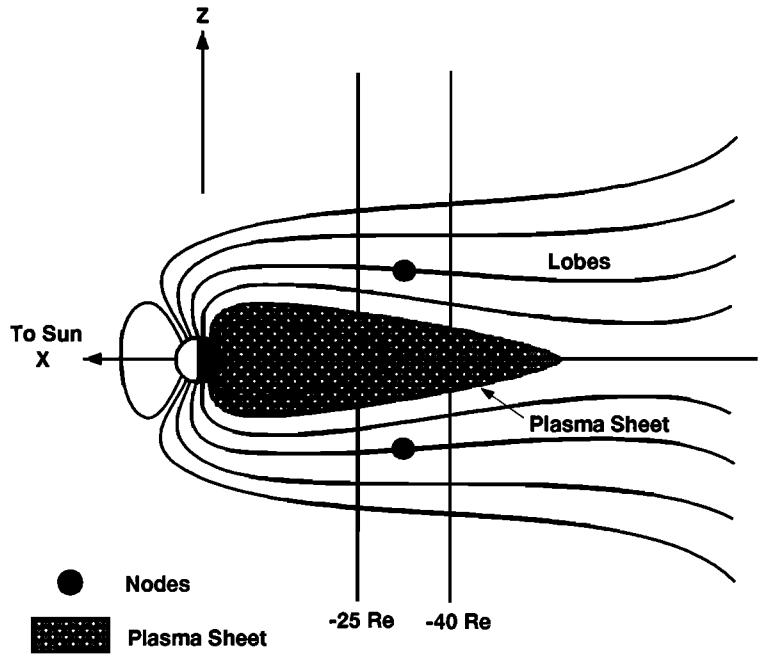

Figure 17. A schematic showing the magnetotail in the *xz* plane. The nodes are seen on the lobe field lines, not at the boundary of the plasma sheet as discussed in the text.

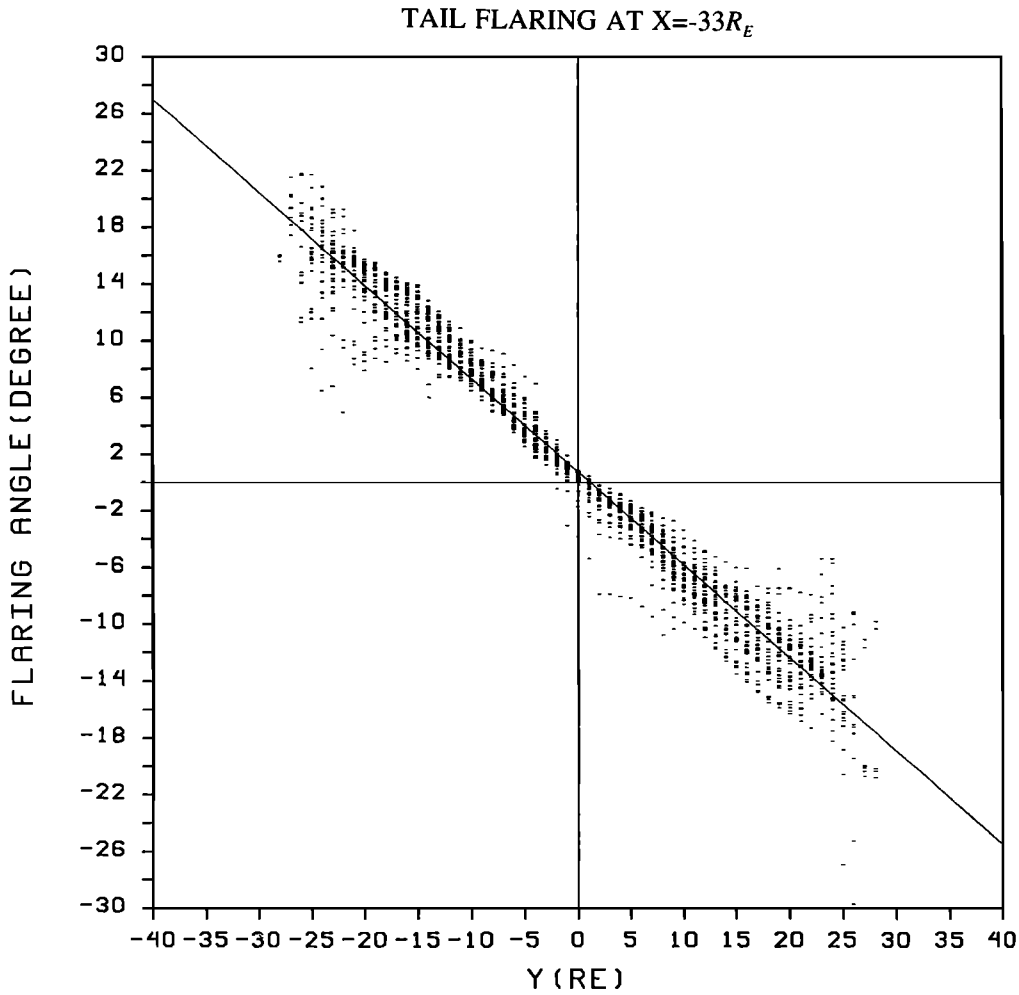

Figure 18. The flaring angles calculated from Figure 9. The line is the least squares fit to the data.

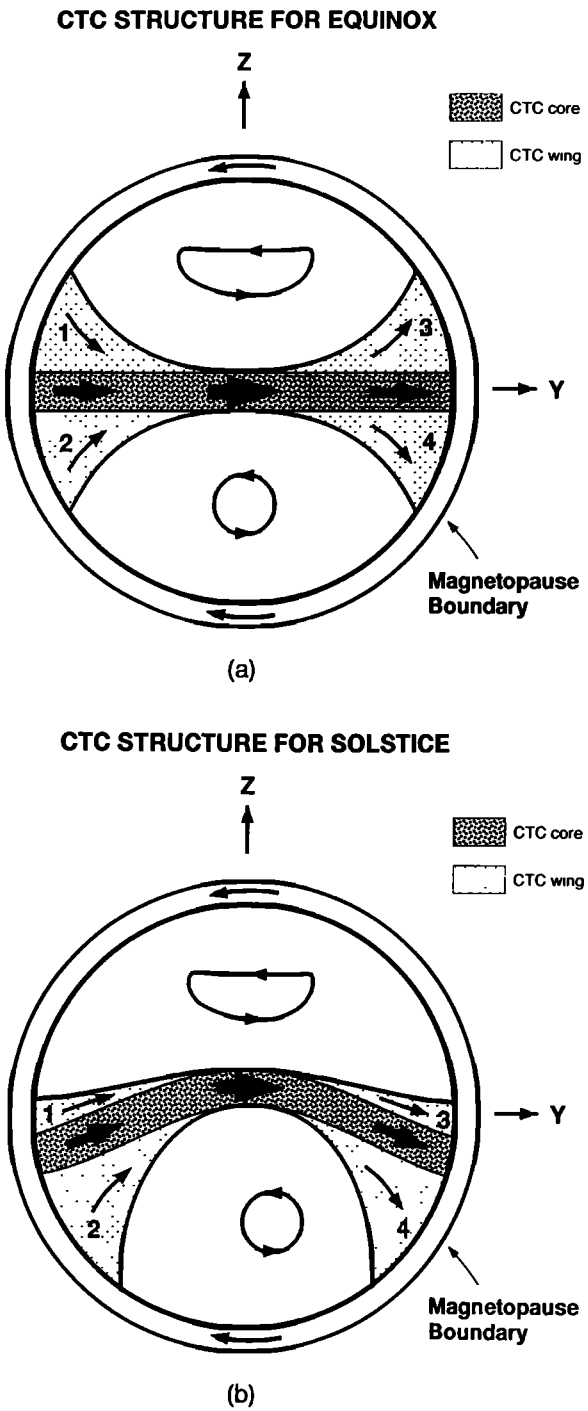

Figure 19. A schematic summarizing the CTC structure for (a) equinox and (b) solstice described in this study.

butterfly. The thickness of the arrows in the center of the current sheet and in the wings illustrates roughly their relative strength. The force maps indicate that the central thickness of the averaged plasma sheet is about $7R_E$. The sketches also show the current vortices and their solstitial asymmetries.

Adding to the number of quantitative formulas for the arc of the neutral sheet is not our object, however. For comparison here, we superimpose Fairfield's displaced ellipse model on the current vector maps (Figure 20). That model fits the current sheet quiet well, but there are discrepancies in addition to those noted by *Hammond et al.* [1994]. In the center the sheet is flatter than the model whereas on the flanks, it hooks backward. The hooking back on the flanks is seen in the Dandouras model but not in the Fairfield and Hammond et al. models.

Another geometrical aspect of the tail connected to dipole tilt is the hinging distance. This is defined as the distance at which the earthward projection of the tail current sheet intersects the magnetic equatorial plane (Figure 21). All but one of the values for the hinging distance in reported studies lie within $2R_E$ of each other. For example, *Russell and Brody* [1967], *Fairfield* [1980], *Hammond et al.* [1994] find hinging distances of $11R_E$, $10.5R_E$, and $9.5R_E$. The exception is *Bowling*'s [1974] study which finds $5.25R_E$. Although he suggests hat the hinging depends on the distance from the Earth, *Russell and Brody* [1967] find no such effect. From the average dipole tilt angle for solstitial months, 23.9°, and the $4R_E$ height of the neutral sheet at midnight, we find $9.9R_E$ for the hinging distance. Not surprisingly, this is close to Hammond et al.'s result, which is based on the same data set, and close to Fairfield's finding. In our study the hinging distance does not change over the range $25R_E < |x| < 40R_E$. Bowling's unusual hinging distance raises the question of whether geomagnetic activity affects the neutral sheet shape and location.

Bowling and Russell [1976] reexamines Bowling's data set to see if increasing or decreasing geomagnetic activity causes smaller hinging distance. They find that the hinging distance appears to be smaller during active times ($Kp \geq 4^-$) than during quiet times ($Kp \leq 2^+$). They suggest that this might explain Bowling's smaller hinging distance for his data are dominated by the high Kp times. *Fairfield* [1980], however, finds little effect of geomagnetic activity on the average location of the hinging distance. Figure 11, showing that geomagnetic activity little affects the current sheet's location, supports Fairfield's conclusion. It also shows that for low Kp the shape of the current sheet is comparatively flat. Nonetheless, the full lifting of the sheet in the center is still present.

Figure 12 shows that the current vectors and stream lines on the equatorial plane are curved toward the Earth. *Speiser and Ness* [1967] report this same sense of curvature. With fewer data, they show that the current vectors are dominantly in the dawn-dusk direction but have a tendency to point sunward on the duskside beyond $15R_E$. Our result extends this picture to both flanks.

Figure 13, showing current density and B_x profiles, addresses the question of the structure and thickness of the current sheet, as distinct from the plasma sheet. Empirically derived estimates of current sheet thickness show a great range depending on position and phase of the substorm life cycle [e.g., *McComas et al.*, 1986; *McPherron*, 1991]. Many of these determinations were made closer to earth than $30R_E$, and were thus more susceptible to substorm effects. *Bowling and Wolf* [1974] conducted the only earlier study comparable to this one in that it was based on averages of measurements taken near x=-$30R_E$. They found an average thickness of $2.5R_E$, which they note would occupy the central third of the plasma sheet. Our finding is similar to this. The central current sheet thickness obtained from the full thickness at half of the peak current density in Figure 13 is about $3R_E$. This $3R_E$ average thickness is about half the plasma sheet average thickness as determined from Figure 16 (as discussed later). Again it must be cautioned that since Figure 13 represents a 16-year average including flapping and oscillatory motions of

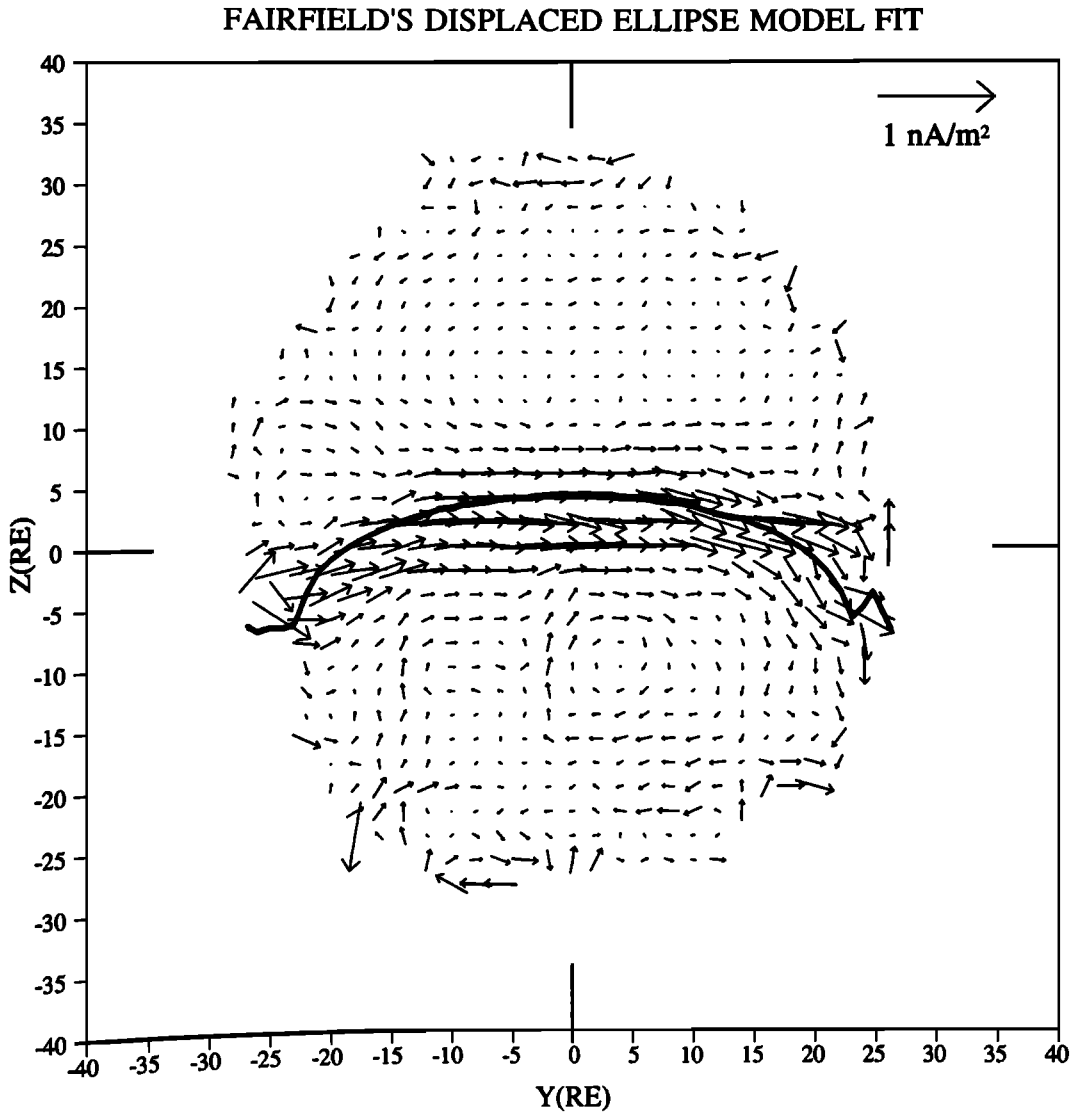

Figure 20. *Fairfield*'s [1980] displaced ellipse model superimposed on the CTC vectors of Figure 7c.

the neutral sheet, IMF effects on the neutral sheet, and substorm disruptions, thickness obtained in case studies could be different than $3R_E$. [e.g., *McComas et al.*, 1986; *McPherron*, 1991].

Next come the field strength contour maps. The main features of the map in Figure 14 of total magnetic field strength are the two hills peaking near 18 nT (average of both lobes) and the intervening valley dipping to 2 nT. That a field depression region coincides with the plasma sheet was reported by *Behannon* [1970] and *Fairfield* [1979]. *Fairfield* [1979, 1986] found that the field strength near the center of the plasma sheet at midnight is about half of its lobe value, that is, 10 nT at the midnight sector. In Figure 14, the minimum field is smaller than this because the magnitude here is an average over the field components whereas *Fairfield*'s [1979, 1986] is an average over the magnitudes. These two methods differ mostly for averages where the vectors are exactly opposite to each other as near the neutral sheet. We also used the second method to determine the total magnitude of the field strength in our data set. It gives 12 nT for the depth of the valley at the midnight sector. This agrees with Fairfield's result, but it is not a good value for the field strength at the midplane. Here we should note that the field magnitudes in the lobes are the same by both methods.

Figure 14 also shows a north-south asymmetry in the field strengths. The peak is about 1 nT weaker in the northern lobe than in the southern lobe. This is close to our determination of error of the mean. However, wider areas of the higher fields in the winter hemisphere suggest that the difference is real. *Meng and Anderson* [1974] studied the magnetic field configuration near $60R_E$ with Explorer 35 data and reported that the field is 2 nT weaker in the northern lobe. This same asymmetry of field strength is evident in *Fairfield*'s [1979] study for $-20R_E < x < -33R_E$. His field is also about 2 nT weaker in the northern than in the southern hemisphere, although he does not draw attention to the difference. *Hammond et al.* [1994] found that the northern and southern lobe field magnitudes agree to within less than 2 nT for all dipole tilt angles. Since they did not consider such differences to be significant, they concluded that the tail lobe field magnitudes are essentially equal.

The same asymmetry shows up in the solstice data set where the difference between the lobe field strengths is about 3 nT. This north-south asymmetry is also reflected in the solstitial

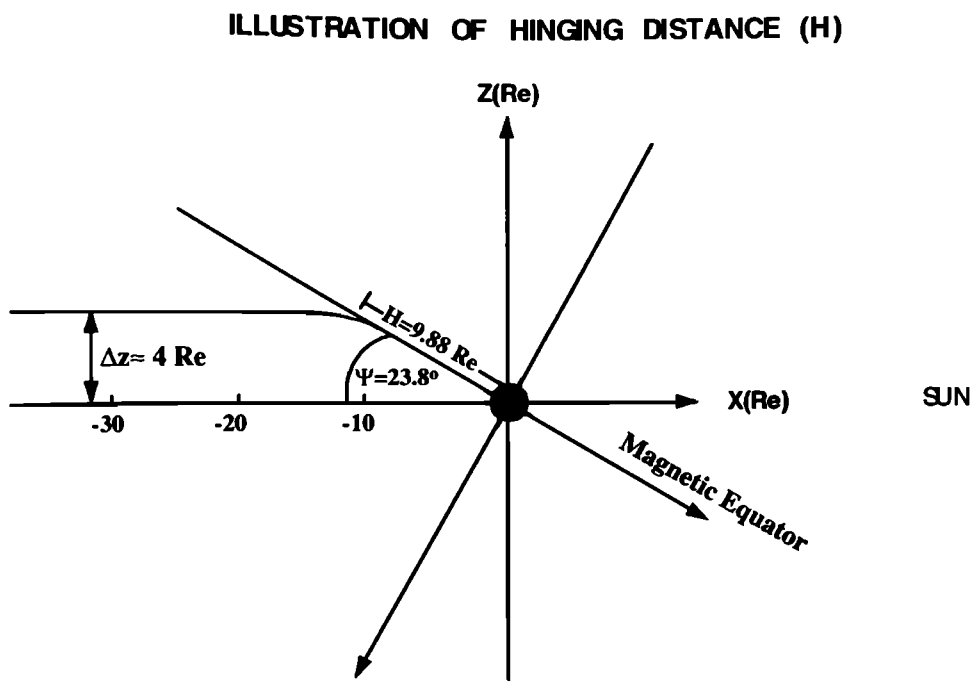

Figure 21. A schematic for defining the hinging distance.

current maps of Figure 10, which show a stronger and more coherent current vortex in the southern hemisphere at the location of the peak in the field strength. These solstitial features are seen for both $Kp \leq 2^+$ and $Kp > 2^+$ and for the x-range of this study from $-25R_E$ to $-40R_E$. In fact, the asymmetry is more pronounced at closer distances and for $Kp < 2^+$. Thus, we interpret the solstitial asymmetry to be real; on average the peak lobe field is stronger in the winter hemisphere.

Relevant to the dawn-dusk asymmetry of the solstitial field strength contours, *Fairfield* [1986] reported a dawn-dusk asymmetry of the B_z component and the total field strength for $x < -10R_E$ and $|z| < 3R_E$. Both are weaker on the dusk sides. He suggested that the dawn-dusk asymmetry of the total field can be caused by the duskward gradient drift of the energetic ions. The same kind of dawn-dusk asymmetry is noticeable in Figure 14 by the duskward shift of the 2-nT contour in the equatorial valley. The opposite sense of dawn-dusk asymmetry is seen in the cross-tail current, however. Both equinox and solstice maps of Figure 10 show that the currents flowing on the dusk-side of the lobes are stronger than on the dawnside. In Figure 14 this asymmetry is seen to be associated with the high field strength regions, especially in the solstice map. These regions are shifted toward dusk in the lobes. That the asymmetry occurs for both seasons and for all Kp levels (see below) shows its reality. Here we should make clear that these asymmetries are not imposed externally by the interplanetary field; such asymmetries would wash out in 16-years averages. The asymmetries of Figure 14 are inherent to the tail.

Geomagnetic activity is another property the field strength contours address. *Mihalov et al.* [1968] and *Behannon* [1970] showed that field strength correlates well with geomagnetic activity as determined by Kp. *Meng and Anderson* [1974] also found that at $60R_E$ the average field strength is about 4 nT higher for $Kp \geq 2^-$ than for $Kp \leq 1^+$. *Fairfield* [1979, 1986] found the field to be a few nanoteslas higher for $AE > 50$ nT both in the tail's center and in the lobes, but especially higher in the center. On the other hand, for $AE < 50$ nT he reported an increase in the dawn-dusk difference in the average field strength and in B_z. Our field strength contours for $Kp > 2^+$ show that the field in the lobes is about 5 nT higher than their quiet time values ($Kp \leq 2^+$). This is about a 25% increase. The midplane value, 2 nT, is unaffected by activity. The north-south asymmetry of the lobe field strengths persists for low Kp. Again, for high Kp, the stronger winter lobe field is larger in area. Thus the field strength is stronger in the winter lobe for all Kp values. The dawn-dusk asymmetry of the total field in the equatorial midplane is more pronounced for $Kp \leq 2^+$, as found by Fairfield, who records that the dawn-dusk differences in field strength is higher for $AE < 50$ nT than for $AE > 50$ nT.

Figure 15 shows that $(\mathbf{JxB})_x$ is relatively uniformly distributed across the plasma sheet, though interestingly the distribution displays three broad peaks, or islands, in both the equinox and solstice maps. This uniformity exists despite the field's becoming more dipolar toward the flanks. Evidently, the increase in B_z toward the flanks compensates for the decrease in cross-tail current in the core. Also, evidently the degree of compensation increases nonlinearly toward the flanks giving the three-island structure.

Figure 16 shows that $|\mathbf{JxB}|_{yz}$ outlines the plasma sheet's borders. The discussion relating to the current profiles shown in Figure 13 concluded that the central peak of the CTC core lies inside the plasma sheet. The point was to estimate the current sheet thickness. Here it is to estimate the plasma sheet thickness. Previously, using plasma data from Vela, *Bame et al.* [1967] found the plasma sheet thickness at the midnight meridian at x=-17R_E to be 4-6R_E. Using IMP 6 magnetic field measurements, *Fairfield* [1979] gave an upper limit of $12R_E$ at midnight between $x = -20R_E$ to $-33R_E$. Figure 16 gives an approximate thickness of $7R_E$ for equinox. This thickness is consistent with the result of *Bame et al.* [1967] and inside Fairfield's upper limit. $|\mathbf{JxB}|_{yz}$ maps give a direct way of de-

termining the plasma sheet boundary from magnetic field measurements. Its use is demonstrated here for the first time.

5. Summary and Conclusions

This paper maps tail magnetic field and current structures and the features identified in them, based on 16 years of averaged magnetic field measurements from IMP 8 near x= -33R_E. These maps show the average picture of the magnetic field and, for the first time, the current configuration of the tail as seen from front, side, and top views. We summarize our findings as follows:

Results from the field maps (field dipolarity, flaring, field line arching-solstice effect):

1. The tail's dipolar field structure toward the dawnside and duskside and the flaring of tail at high latitudes are seen directly in the cross-sectional vector maps and field lines of the magnetic field. The flaring of the tail in the east-west direction is -0.656°/R_E at x = -33R_E and the aberration angle is 3° (Figures 7, 8, 9, and 18).

2. The nodes in the field pattern lie in the lobes. This shows that the plasma sheet boundary lies on the field lines converging toward the tail axis (Figures 7a, 7b, and 17).

3. At solstices the magnetic field lines arch above the equatorial plane in the middle and dip below it on the flanks owing to the Earth's dipole tilt. The nodes are found to be raised above the equator by about 3R_E at midnight (Figures 7c, 7d, and 8).

Results from the current maps (CTC shape, thickness, warping, *Kp* effect, asymmetries):

4. The cross-tail current (CTC) system has distinct core and wing parts. The core forms the strongest current density part of the CTC and extends as a bar from dawn to dusk in the tail's center. The wings have smaller current densities and extend to about |z| = 20R_E on the dawnside and duskside, thus giving CTC a bow tie appearance (Figures 10 and 19).

5. The "vertical" profile of current density through the core of the CTC in the midnight sector shows a head-and-shoulders structure (a strong central peak and flanking shoulders) as also demonstrated by *McComas et al.* [1986]. Nonetheless, the B_x profile is well represented by a Harris sheet with a thickness of 7R_E. The central peak of the current sheet is 3R_E in full-thickness at half maximum. (Figures 11, 13, and 16).

6. The dipole tilt influence on the current sheet is seen directly. The CTC core rises above the GSM equator by about 4R_E in the tail's center and dips below it by about 7R_E on the flanks. *Fairfield*'s [1980] displaced ellipse model well represents the warping of the current but the middle of the current sheet seems flatter than in the model (Figures 8, 10a, 10b, 13, and 20).

7. There are well-defined current vortices in the lobes. The strength and the location of these vortices show a dawn-dusk and also north-south asymmetry. The center of current vortices is shifted to the duskward in both lobes; therefore the current density is stronger on the dusk than on the dawnside. The winter current vortex is strongest (Figures 10).

8. The solstitial hinging of the current sheet remains unchanged for high *Kp* ($Kp \geq 2^+$) and for low *Kp* ($Kp \leq 2^+$). The warping is pronounced for high *Kp*. The north-south and dawn-dusk asymmetries are also found for all *Kp* level (Figure 11).

9. The current stream lines in the xy plane are convex earthward. The radius of curvature is greater than the distance to the Earth and increases with *Kp* (Figure 12).

Results from the contour maps (field strength topology, asymmetries, $(\mathbf{JxB})_x$, and $|\mathbf{JxB}|_{yz}$):

10. The magnetic field strength dips to 2 nT at the center of the current sheet and peaks at 18 nT in the lobes. For solstice the field strength is about 3 nT stronger in the winter lobe and the field contours are shifted to the duskside of the tail in both lobes. A dawn-dusk asymmetry also exist in the equatorial tail as noted by *Fairfield* [1986]. The field strength is weaker on the duskside than on the dawnside (Figure 14).

11. The $(\mathbf{JxB})_x$ contours are nearly uniform across the plasma sheet. Nonetheless, they exhibit three peaks corresponding to the flanks and the center, but shifted duskward (Figure 15).

12. The plasma sheet is found to be 7R_E thick as determined by the $|\mathbf{JxB}|_{yz}$ peaks. The largest values occur in the center but shifted duskward (Figure 16).

Acknowledgments. This research was supported by the National Science Foundation under grant ATM 91-17484 (University of California, Los Angeles). We wish to thank the Goddard Space Flight Center magnetic field data processing team for their support over the many years covered by these data, especially Bill Mish, Frank Ottens, Sharon Beckwith, and Phyllis Hodge.

The editor thanks R.C. Elphic and T.I. Pulkkinen for their assistance in evaluating this paper.

References

Bame, S.J., J.R. Asbridge, H.E. Felthauser, E.W. Hones, and I.B. Strong, Charateristics of the plasma sheet in the Earth's magnetotail, *J. Geophys. Res.*, *72*, 113, 1967.

Behannon, K.W., Geometry of the geomagnetic tail, *J. Geophys. Res.*, *75*, 743, 1970.

Bowling, S.B., The influence of the direction of the geomagnetic dipole on the position of the neutral sheet, *J. Geophys. Res.*, *79*, 5155, 1974.

Bowling, S.B., and C.T Russell, The position and shape of the neutral sheet at 30R_e distance, *J. Geophys. Res.*, *81*, 270, 1976.

Bowling, S.B., and R.A. Wolf, The motion and magnetic structure of the plasma sheet near 30R_e, *Planet. Space Sci.*, *22*, 673, 1974.

Dandouras, J., On the average shape and position of the geomagnetic neutral sheet and it influence on the plasma sheet statistical studies, *J. Geophys. Res.*, *93*, 7345, 1988.

Fairfield, D.H., On the average configuration of the geomagnetic tail, *J. Geophys. Res.*, *84*, 1950, 1979.

Fairfield, D.H, A statistical determination of the shape and position of the geomagnetic neutral sheet, *J. Geophys. Res.*, *85*, 775, 1980.

Fairfield, D.H, The magnetic field of the equatorial magnetotail from 10 to 40 R_e, *J. Geophys. Res.*, *91*, 4238, 1986.

Fairfield, D.H. and N.F. Ness, Configuration of the geomagnetic tail during substorms, *J. Geophys. Res.*, *75*, 7032, 1970.

Gosling, J.T., D.J. McComas, M.F. Thomsen, S.J. Bame, and C.T. Russell, The warped neutral sheet and plasma sheet in the near-Earth geomagnetic tail, *J. Geophys. Res.*, *91*, 7093, 1986.

Hammond, C.M., M.G. Kivelson, and R.J. Walker, Imaging the effect of the dipole tilt on magnetotail boundaries, *J. Geophys. Res.*, in press, 1994.

Harris, E.G., On a plasmaseparating regions of oppositely directed magnetic field, *Nuovo Cimento, XXIII*, 1, 1962.

McComas, D.J., C.T. Russell, R.C. Elphic, and S.J. Bame, The near-Earth cross-tail current sheet: Detailed ISEE-1 and 2 case studies, *J. Geophys. Res.*, *91*, 4287, 1986.

McPherron, R.L., Physical processes producing magnetospheric substorms and magnetic storms, in *Geomagnetism*, edited by J. A. Jacobs, p. 593, Academic, San Diego, Calif., 1991.

Meng, C.-I., and K.A. Anderson, Magnetic field configuration in the magnetotail near 60R_E, *J. Geophys. Res.*, *79*, 5143, 1974.

Mihalov, J.D., D.S. Colburn, R.G. Currie, and C.P. Sonett, Configuration and reconnection of the geomagnetic tail, *J. Geophys. Res.*, *73*, 3, 1968.

Murayama, T., Spatial distribution of energetic electrons in the geomagnetic tail, *J. Geophys. Res.*, *71*, 5547, 1966.

Ness, N.F., The Earth's magnetic tail, *J. Geophys. Res.*, *70*, 2989, 1965.

Ohtani, S., and S. Kokubun, IMP 8 magnetic field observation of the high latitude tail boundary: Locations and force balance, *J. Geophys. Res.*, *93*, 9709, 1990.

Russell, C.T., and K.J. Brody, Some remarks on the position and shape of the neutral sheet, *J. Geophys. Res.*, *72*, 6104, 1967.

Speiser, T.W., and N.A. Ness, The neutral sheet in the Geomagnetic tail: Its motion, equivalent currents, and field line connection through it, *J. Geophys. Res.*, *72*, 131, 1967.

Tsyganenko, N.A., A magnetospheric magnetic field model with a warped tail current sheet, *Planet. Space Sci.*, *37*, 5, 1989.

Tsyganenko, N.A., Quantitative models of the magnetospheric magnetic field: Methods and results, *Space Sci. Rev.*, *54*, 75, 1990.

Voigt, G.-H., The shape and position of the plasma sheet in Earth's magnetotail, *J. Geophys. Res.*, *89*, 2169, 1984.

Voigt, G.-H., and R.V. Hilmer, The influence of the IMF B_y component on the Earth's magneto-hydrostatic magnetotail, in *Magnetotail Physics*, edited by A. T. Lui, p. 91, John Hopkins University, Baltimore, Maryland, 1987.

Walker, R.J., T. Ogino, and M. Ashour-Abdalla, Simulating the magnetosphere: The structure of the magnetotail, in *Solar System Plasma Physics*, Geophys. Monogr. Ser., vol. 54, edited by J. H. Waite, Jr, J. L. Burch, and R. L. Moore, p. 61, AGU, Washington, D. C., 1989.

Z. Kaymaz and G. L. Siscoe, Center for Space Physics, Boston University, 725 Commonwealth Avenue, Boston, MA 02215. (e-mail: SPAN.buasta::zerefsan; SPAN.buasta::siscoe)

R. P. Lepping and N. A. Tsyganenko, NASA Goddard Space Flight Center, Greenbelt, MD 20770 (e-mail: SPAN.lepvax::u5rpl, SPAN.lepvax::ys2nt)

(Received August 3, 1993; revised December 1, 1993;
accepted December 21, 1993.)